

GA-A28239

# **TGLF RECALIBRATION FOR ITER STANDARD CASE PARAMETERS FY2015**

**Theory & Simulation Performance Target Final Report**

by  
**J. CANDY**

Prepared for the  
U.S. Department of Energy  
under Contract No. DE-FG02-95ER54309

**DATE PUBLISHED: DECEMBER 2015**



## **DISCLAIMER**

This report was prepared as an account of work sponsored by an agency of the United States Government. Neither the United States Government nor any agency thereof, nor any of their employees, makes any warranty, express or implied, or assumes any legal liability or responsibility for the accuracy, completeness, or usefulness of any information, apparatus, product, or process disclosed, or represents that its use would not infringe privately owned rights. Reference herein to any specific commercial product, process, or service by trade name, trademark, manufacturer, or otherwise, does not necessarily constitute or imply its endorsement, recommendation, or favoring by the United States Government or any agency thereof. The views and opinions of authors expressed herein do not necessarily state or reflect those of the United States Government or any agency thereof.

GA-A28239

# **TGLF RECALIBRATION FOR ITER STANDARD CASE PARAMETERS FY2015**

**Theory & Simulation Performance Target Final Report**

by  
**J. CANDY**

Prepared for the  
U.S. Department of Energy  
under Contract No. DE-FG02-95ER54309

**GENERAL ATOMICS PROJECT 03726  
DATE PUBLISHED: DECEMBER 2015**



# 1 Executive Summary

## Early observations

This work was motivated by the observation, as early as 2008<sup>1</sup>, that GYRO [1] simulations of some ITER operating scenarios exhibited nonlinear zonal-flow generation large enough to effectively quench turbulence inside  $r/a \sim 0.5$ . This observation of flow-dominated, low-transport states persisted even as more accurate and comprehensive predictions of ITER profiles were made using the state-of-the-art TGLF transport model [2]. This core stabilization is in stark contrast to GYRO-TGLF comparisons for modern-day tokamaks, for which GYRO and TGLF are typically in very close agreement [3, 4, 5]. So, we began to suspect that TGLF needed to be generalized to include the effect of zonal-flow stabilization in order to be more accurate for the conditions of reactor simulations. While the precise cause of the GYRO-TGLF discrepancy for ITER parameters was not known, it was speculated that closeness to threshold in the absence of driven rotation, as well as electromagnetic stabilization<sup>2</sup>, created conditions more sensitive to the self-generated zonal-flow stabilization than in modern tokamaks.

## Need for nonlinear zonal-flow stabilization

To explore the inclusion of a zonal-flow stabilization mechanism in TGLF, we started with a nominal ITER profile predicted by TGLF, and then performed linear and nonlinear GYRO simulations to characterize the behavior at and slightly above the nominal temperature gradients for finite levels of energy transport. Then, we ran TGLF on these cases to see where the discrepancies were largest. The predicted ITER profiles were indeed near to the TGLF threshold over most of the plasma core in the hybrid discharge studied (weak magnetic shear,  $q > 1$ ). Scanning temperature gradients above the TGLF power balance values also showed that TGLF overpredicted the electron energy transport in the low-collisionality ITER plasma. At first (in Q3), a model of only the zonal-flow stabilization (Dimits shift) was attempted. Although we were able to construct an *ad hoc* model of the zonal flows that fit the GYRO simulations, the parameters of the model had to be tuned to each case. A physics basis for the zonal flow model was lacking.

## Electron energy transport at short wavelength

A secondary issue – the high- $k$  electron energy flux – was initially assumed to be independent of the zonal flow effect. However, detailed studies of the fluctuation spectra from recent multiscale (electron and ion scale) GYRO simulations [6] provided a critical new insight into the role of zonal flows. The multiscale simulations suggested that advection by the zonal flows strongly suppressed electron-scale turbulence. Radial shear of the zonal  $\mathbf{E} \times \mathbf{B}$  fluctuation could not compete with the large electron-scale linear growth rate, but the  $k_x$ -mixing rate of the  $\mathbf{E} \times \mathbf{B}$  advection could. This insight led to a preliminary new model for the way zonal flows saturate **both** electron and ion-scale turbulence. It was also discovered that the strength of the zonal  $\mathbf{E} \times \mathbf{B}$  velocity could be computed from the linear growth rate spectrum. The new saturation model (SAT1),

---

<sup>1</sup>J. Candy, “Progress on TGYRO: The Steady-state Gyrokinetic Transport Code”, TTF 2008 poster, Boulder, CO

<sup>2</sup>J. Candy, “Gyrokinetic Eigenmode Analysis of High-Beta Shaped Plasmas”, APS 2010 poster, Chicago, IL

which replaces the original model (SAT0), was fit to the multiscale GYRO simulations as well as the ion-scale GYRO simulations used to calibrate the original SAT0 model. Thus, SAT1 captures the physics of both multiscale electron transport and zonal-flow stabilization. In future work, it the SAT1 model will require significant further testing and (expensive) calibration with non-linear multiscale gyrokinetic simulations over a wider variety of plasma conditions – certainly more than the small set of scans about a single C-Mod L-mode discharge. We believe the SAT1 model holds great promise as a physics-based model of the multiscale turbulent transport in fusion devices.

**Correction to ITER performance predictions** Finally, the impact of the SAT1 model on the ITER hybrid case is mixed. Without the electron-scale contribution to the fluxes, the Dimits shift makes a significant improvement in the predicted fusion power as originally posited. Alas, including the high- $k$  electron transport reduces the improvement, yielding a modest net increase in predicted fusion power compared to the TGLF prediction with the original SAT0 model.

# Contents

<b>1</b>	<b>Executive Summary</b>	<b>3</b>
<b>2</b>	<b>Background and Motivation</b>	<b>6</b>
2.1	Physics Issues . . . . .	6
2.2	Performance Target and Milestones . . . . .	8
<b>3</b>	<b>Preliminary Linear and Nonlinear Analysis</b>	<b>9</b>
3.1	Local parameters for generic ITER scenarios . . . . .	9
3.2	Linear scans over near-threshold region . . . . .	10
3.3	Preliminary nonlinear simulations (Q1) . . . . .	14
<b>4</b>	<b>Nonlinear simulations for recalibration (Q2)</b>	<b>17</b>
<b>5</b>	<b>TGLF Recalibration</b>	<b>19</b>
5.1	Comparison of TGLF with the 72 GYRO Q2 ITER Simulations . . . . .	19
5.2	Equal-temperature, circular nonlinear GYRO Q3 Simulations . . . . .	19
5.3	The Dimits Shift Regime . . . . .	20
5.4	Initial recalibration attempt . . . . .	22
5.5	Multiscale impacts on ITER and final GYRO Q4 simulations . . . . .	22
5.6	Properties of the electric potential turbulence spectrum . . . . .	25
5.7	ITER Profile Prediction . . . . .	35
<b>6</b>	<b>Discussion</b>	<b>37</b>
6.1	Final Calibration Check via GYRO Comparisons . . . . .	37
<b>7</b>	<b>Appendix: Summary of GYRO Q2 nonlinear simulations</b>	<b>39</b>

## 2 Background and Motivation

Development of an experimentally validated, predictive integrated modeling capability is a key objective of the US fusion energy program. Fundamental to any such predictive modeling of magnetic-confinement based fusion devices such as tokamaks is the need for an accurate model describing the small-scale, gradient-driven plasma microturbulence and its associated cross-field transport. As this transport determines the relationship between the equilibrium kinetic pressure and current profiles of the plasma and various heating sources (both internal and external), and thus the level of confinement achieved, predictions of fusion gain in any future device will depend sensitively on the accuracy of the transport model used. Recognizing the importance of these models for predictions of ITER performance, a 2015 Fusion Energy Science (FES) theory and simulation performance target has been defined to advance a key issue for predictive modeling of future reactors.

### 2.1 Physics Issues

Currently, the quasilinear Trapped Gyro-Landau-Fluid (TGLF) code [2] provides the première transport model for profile prediction in integrated modeling studies of future fusion reactors. However, the current calibration of TGLF [7, 8, 9] is based upon nonlinear GYRO [1] simulations which used baseline parameters for which the magnetic safety factor  $q$  was well above unity and plasma gradients well above the linear threshold (i.e., critical) values. Moreover, only a small fraction of the simulations in the GYRO Transport Database (<https://fusion.gat.com/theory-wiki/gyro/gyro-database.pdf>) used to calibrate TGLF include electromagnetic effects, which are now believed to play an important role in reactor-relevant burning plasma regimes.

Past experience (in unpublished work) with comparisons of GYRO simulations to TGLF computed fluxes have shown repeatedly that TGLF may overpredict fluxes and therefore underpredict performance in the reactor core where  $q$  is low and the turbulence is very close to the linear threshold. Two possible reasons for the overprediction of the GYRO fluxes by TGLF in this regime are related to TGLF underpredicting (a) the linear gyrokinetic thresholds for onset of ion temperature gradient (ITG) and trapped electron modes (TEM), particularly due to electromagnetic effects, and/or (b) the stabilizing effects arising from self-generated zonal flows [10]. With particular regard to point (b), the TGLF approach does not explicitly include zonal-flow effects anywhere in its saturation model. These effects are included indirectly through the GYRO Transport Database simulations (which do include these effects) that TGLF is calibrated against.

ITER modeling [11] has shown that acceptable confinement requires core ion/electron energy fluxes to be on the order of a single gyroBohm; that is,  $Q_e/Q_{GB}, Q_i/Q_{GB} \simeq 1$ , where  $Q_{GB} \doteq n_e T_e c_s (\rho_s/a)^2$  is the gyroBohm energy flux,  $\rho_s$  is the ion-sound gyroradius, and  $a$  is the mid-plane minor radius of the last closed flux surface. In cases with low levels of equilibrium ro-

tational shear, previous experience implies this level of transport corresponds to a close proximity to the linear threshold, and GYRO [1] simulations show that nonlinearly-generated zonal flows are very active under these conditions and lead to turbulence suppression (the so-called “Dimits-shift” regime [12]) and bursty (intermittent) transport. Linear and nonlinear gyrokinetic simulation under these conditions are also more problematic and challenging in comparison to cases that sit well above threshold, due to the challenges in obtaining well-converged near-zero growth rates, and statistically robust estimates of (time-averaged) mean transport levels.

In the baseline case studied in this report, we observe that for steady-state ITER profiles predicted by TGLF, GYRO simulations do exhibit weak linear instability, but with turbulence subsequently reduced by zonal-flow activity at radii inside about  $r/a = 0.6$  (where  $r$  is the half-width of the flux surface). This observation suggests that a better accounting for electromagnetic critical gradients and nonlinear zonal-flow stabilization in TGLF might lead to improved ITER performance predictions. Thus for the purpose of reactor modeling we are motivated to design new benchmark/calibration cases for TGLF suitable for reactor parameters, and then subsequently recalibrate TGLF in this regime.

All profile predictions herein are made using the TGYRO transport solver [13], based on an ITER hybrid DT scenario with approximately 45 MW of auxiliary power, hollow  $q$ -profile, equal D/T fractions, and thermal  $^4\text{He}$  ash. Impurity ions (Ar, Be, W) and fast-ion populations are also retained in the most complete scenario definition, but we have established that neglect of these species during TGYRO simulation leads to only small errors in profile prediction. For this reason, we consider only three gyrokinetic ions (D, T,  $^4\text{He}$ ) in the subsequent modeling. In TGYRO, alpha heating to electrons and ions, collisional exchange, and electron radiation are computed self-consistently. Neoclassical transport for all species is computed by NEO [14, 15] without approximation. Using 8 TGYRO simulation radii (plus a point on the magnetic axis at which fluxes equal zero exactly), we compute steady-state temperature profiles such that the corresponding gradients serve as nominal ones. The total alpha (fusion) power for this case, inside  $r/a = 0.8$ , is 102 (510) MW. This prediction uses unmodified TGLF as the transport model, with no direct reference to GYRO simulations. In what follows we define  $z_i \doteq -(a/T_i)dT_i/dr$  and  $z_e \doteq -(a/T_e)dT_e/dr$ .

## 2.2 Performance Target and Milestones

Below, we summarize the official performance target, together with the four quarterly milestones.

*Perform massively parallel plasma turbulence simulations to determine expected transport in ITER. Starting from best current estimates of ITER profiles, the turbulent transport of heat and particles driven by various micro-instabilities (including electromagnetic dynamics) will be computed. Stabilization of turbulence by nonlinear self-generated flows is expected to improve ITER performance, and will be assessed with comprehensive electromagnetic gyrokinetic simulations.*

**1** *Perform linear analysis of ITER standard scenario and preliminary local nonlinear runs at sequence of minor radii. These runs will use the nominal profiles calculated using the current version of TGLF. Three kinetic ion species will be used (D,T, He ash) and the energetic ions will be treated as a dilution.*

**2** *Define a reduced case (electrostatic, single kinetic ion) that is representative of the ITER scenario in 1. Perform large series of parameter scans for this reduced case, including nonlinear q-scans. These scans will be used to recalibrate TGLF to include the stabilizing effect of nonlinear self-generated (zonal) flows.*

**3** *Carry out TGLF recalibration and, using the recalibrated TGLF in TGYRO, recompute best correction to nominal ITER profiles.*

**4** *Perform nonlinear GYRO simulations on the recomputed profiles. In particular, assess the effects of transverse and compressional electromagnetic effects, helium concentration and trace high-Z impurities.*

### 3 Preliminary Linear and Nonlinear Analysis

#### 3.1 Local parameters for generic ITER scenarios

At the radii  $r/a = (0.4, 0.5, 0.6)$  we summarize the required local parameters for turbulence simulations. The nominal local gradients are those predicted by TGYRO-TGLF-NEO predictive simulation. The aim of this work is to recalibrate TGLF for gradients close to and above this range and, ultimately, repredict ITER performance after recalibration.

Table 1: ITER Scenario Local Geometric Parameters

Local parameter	$r/a = 0.4$	$r/a = 0.5$	$r/a = 0.6$
$\rho_{\text{tor}}$	0.3613	0.4531	0.5480
$R_0/a$	3.2384	3.2232	3.2051
$q$	1.5688	1.6961	1.8838
$s$	0.2253	0.4728	0.6833
$\kappa$	1.5076	1.5074	1.5194
$s_\kappa$	-0.0218	0.0218	0.0689
$\delta$	0.0732	0.0930	0.1176
$s_\delta$	0.0698	0.1098	0.1617
$-\Delta$	0.1385	0.1664	0.1942
$B_{\text{unit}}(T)$	7.6724	7.9257	8.2809

Table 2: ITER Scenario Profile Parameters

Local parameter	$r/a = 0.4$	$r/a = 0.5$	$r/a = 0.6$
$T_i/T_e$	0.9698	0.9731	0.9719
$\beta_{e,\text{unit}}(\%)$	1.0638	0.8652	0.6871

Table 3: ITER Scenario Nominal Gradients

Local parameter	$r/a = 0.4$	$r/a = 0.5$	$r/a = 0.6$
$a/L_n$	0.2696	0.2276	0.3429
$a/L_{Ti}$	1.1301	1.1379	1.1748
$a/L_{Te}$	1.2262	1.1096	1.1776

### 3.2 Linear scans over near-threshold region

Below we summarize linear scans carried out to characterize core stability boundaries. The scans are shown in Figs. 1, 2 and 3. We remark that near-threshold linear simulations are challenging because eigenmodes become very extended along a fieldline and require increased poloidal resolution. To this end, a sample eigenmode is shown in Fig. 4. In addition, slowly-growing modes take a long time to converge in initial-value simulation, or are subject to velocity-integration inaccuracy in eigenvalue simulation as the pole corresponding to the marginal mode approaches the real axis.

We focus on three radii:  $r/a = (0.4, 0.5, 0.6)$ , and two wavenumbers:  $k_\theta \rho_s = (0.3, 0.5)$ . The local parameters corresponding to each of the three radii are summarized in Tables 1-3. For each of these six cases we run GYRO (1) electrostatically, (2) with transverse electromagnetic fluctuations, and (3) with transverse and compressional electromagnetic fluctuations. The TGLF linear results are limited to the first two cases.

**Conclusion:** In virtually every case considered, significant differences are observed between the GYRO and TGLF predictions of the threshold critical gradient for instability (defined qualitatively as either where the growth rate reaches zero exactly, or exhibits a sharp inflection point at near-zero values), as well as between the electrostatic and electromagnetic GYRO predictions. In general, GYRO observes a stronger stabilizing effect from inclusion of transverse magnetic fluctuations (finite  $A_\parallel$ ) than TGLF does. However, inclusion of compressional physics (finite  $B_\parallel$ ) is universally seen to be destabilizing, and non-negligible, in some cases almost completely balancing the stabilization induced by the transverse fluctuations. These results provide strong support for the hypothesis advanced in the introduction, that at least some fraction of the difference between the TGLF and GYRO predictions (even in the electrostatic limit) can be explained by differences in linear critical gradients predicted by the models. Moreover, they suggest that electromagnetic effects will need to be carefully considered in the nonlinear simulations to gain the most accurate predictions, which may well raise new challenges associated with “subcritical  $\beta$ ” effects. Given that significantly increased resolution (relative to standard settings) was needed to obtain converged GYRO results, the possibility remains that the TGLF predictions can be brought into better agreement with GYRO using increased resolution as well.

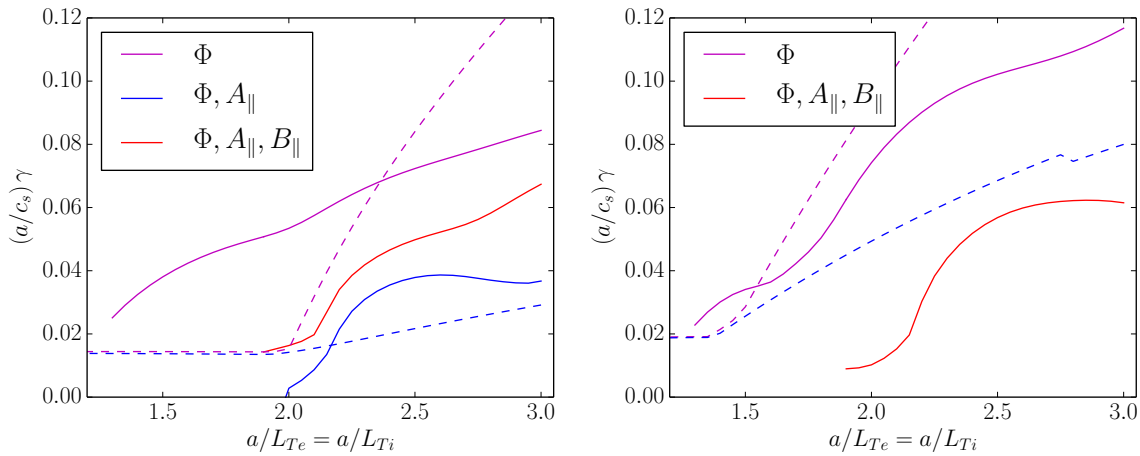


Figure 1: GYRO linear eigenvalues at  $r/a = 0.4$  showing approach to linear threshold as gradients are decreased. Left panel shows  $k_\theta \rho_s = 0.3$  and right panel shows  $k_\theta \rho_s = 0.5$ . GYRO simulations are shown as solid curves, whereas TGLF results are given as dashed curves. The region below about  $(a/c_s) \gamma \sim 0.05$  is very difficult to resolve numerically and is subject to some error.

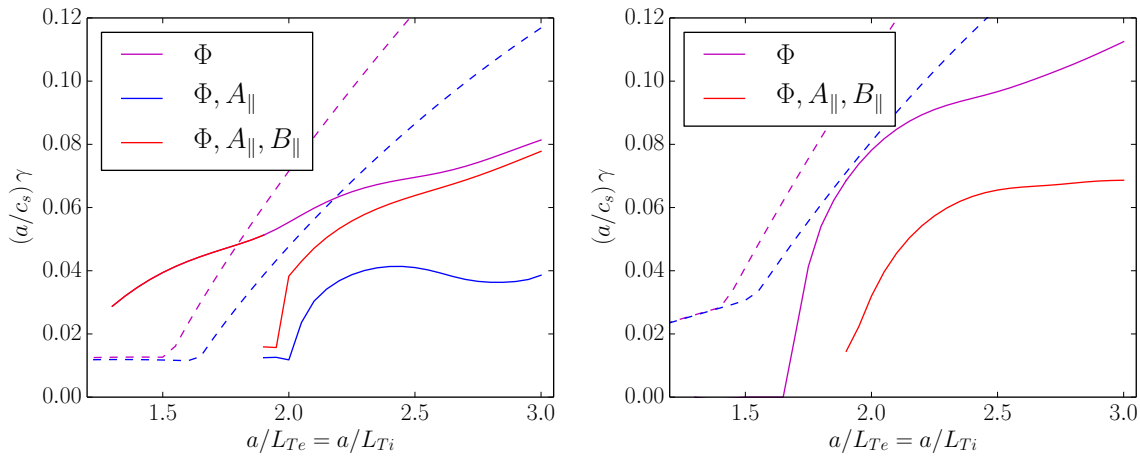


Figure 2: Linear eigenvalues at  $r/a = 0.5$  showing approach to linear threshold as gradients are decreased. Left panel shows  $k_\theta \rho_s = 0.3$  and right panel shows  $k_\theta \rho_s = 0.5$ . GYRO simulations are shown as solid curves, whereas TGLF results are given as dashed curves. The region below about  $(a/c_s) \gamma \sim 0.05$  is very difficult to resolve numerically and is subject to some error.

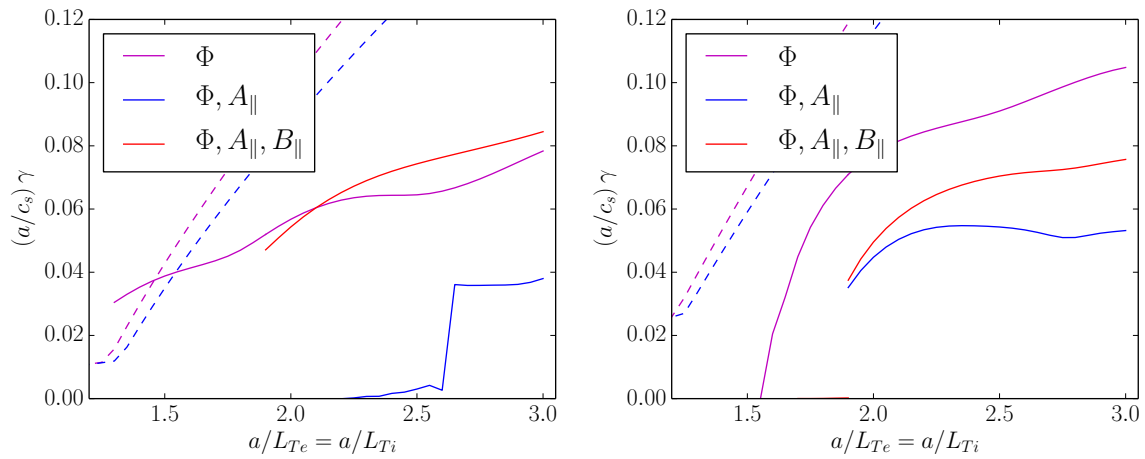


Figure 3: Linear eigenvalues at  $r/a = 0.6$  showing approach to linear threshold as gradients are decreased. Left panel shows  $k_\theta \rho_s = 0.3$  and right panel shows  $k_\theta \rho_s = 0.5$ . GYRO simulations are shown as solid curves, whereas TGLF results are given as dashed curves. The region below about  $(a/c_s)\gamma \sim 0.05$  is very difficult to resolve numerically and is subject to some error.

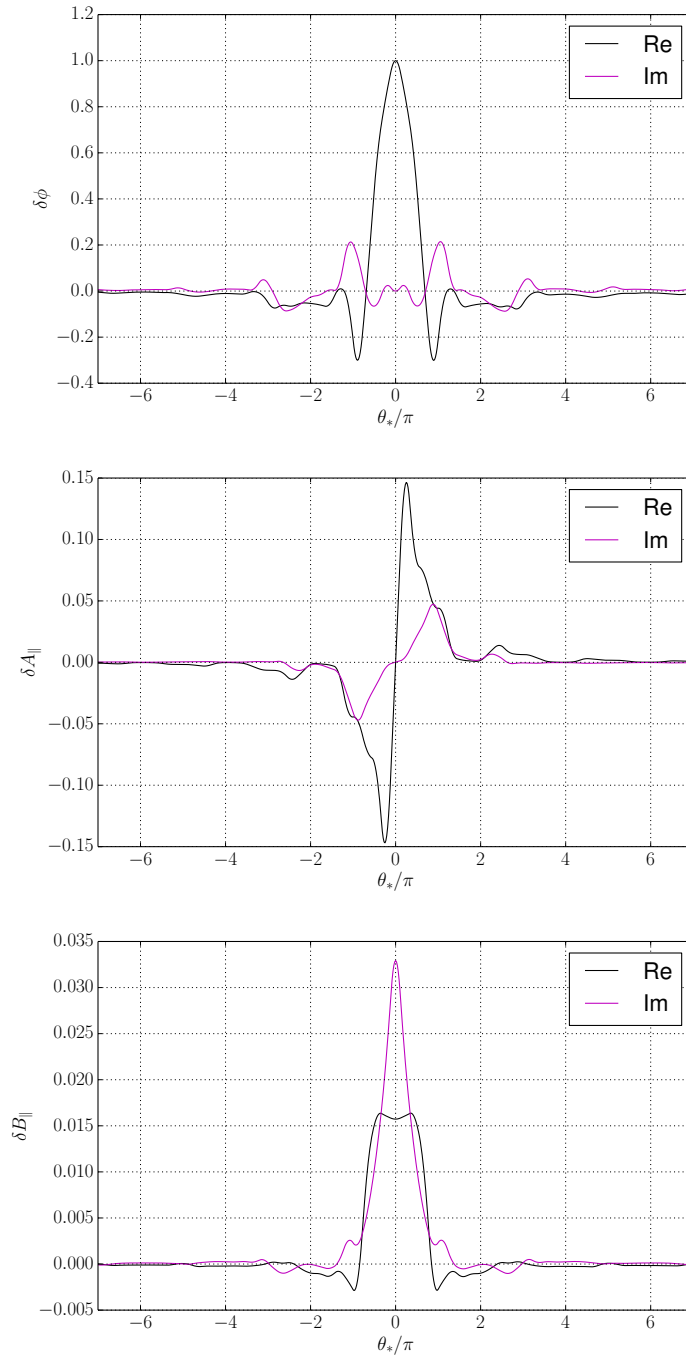


Figure 4: Linear modes structures for the  $\Phi$ ,  $A_{\parallel}$  and  $B_{\parallel}$  components of the eigenmode at  $r/a = 0.5$  and  $k_{\theta}\rho_s = 0.3$ . Gradients are close to marginal at  $a/L_{Ti} = a/L_{Te} = 2.1$

### 3.3 Preliminary nonlinear simulations (Q1)

Below we summarize preliminary nonlinear simulations based on initial profiles generated for ITER and summarized in Tables 1, 2 and 3. Nonlinear simulations in the near-threshold regime are tedious because – as will be clearly illustrated – the associated turbulence is bursty (intermittent) requiring very-long-time simulations to compute a reasonable average. Moreover, obtaining grid convergence is more troublesome since transport become very sensitive to resolution in essentially every dimension. Specifically, two simulations at  $r/a = 0.4$  are shown in Figs. 5 and 6, one simulation at  $r/a = 0.5$  is shown in Fig. 7 and one at  $r/a = 0.6$  is shown in Fig. 8.

**Conclusion:** In every case, the simulations must be run to  $t \geq 1500a/c_s$  – a factor of 5-10 longer than for typical current-day devices – before reaching something that may plausibly be considered a reasonable statistical average relevant for benchmarking against other model predictions. Moreover, in each case, the GYRO predictions of the electron heat fluxes are a factor of 2 or more smaller than the equivalent TGLF predictions, with similar underpredictions of the ion heat fluxes at  $r/a = 0.4$  and 0.5. As these were preliminary simulations, only three thermal ion species (D, T,  $^4\text{He}$ ) were used and a number of physics effects (electromagnetic fluctuations, collisions, and equilibrium  $\mathbf{E} \times \mathbf{B}$  shear) were neglected. While neglect of collisions,  $\mathbf{E} \times \mathbf{B}$  shear, and dynamical treatments of the heavy impurity and fast  $^4\text{He}$  ions is supported by previous observations, electromagnetic effects are expected to have a significant effect on these predictions (for both TGLF and GYRO), based upon the linear studies in the previous section.

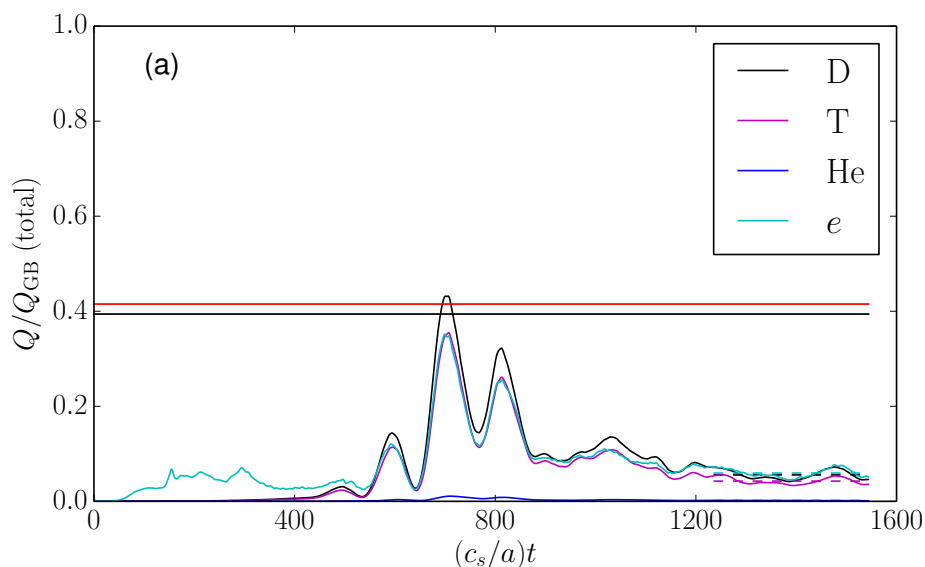


Figure 5: GYRO nonlinear simulation at  $r/a = 0.4$ . TGLF results for electron and ion fluxes are shown in red and black lines, respectively. Gradients are the nominal values shown in Table 3.

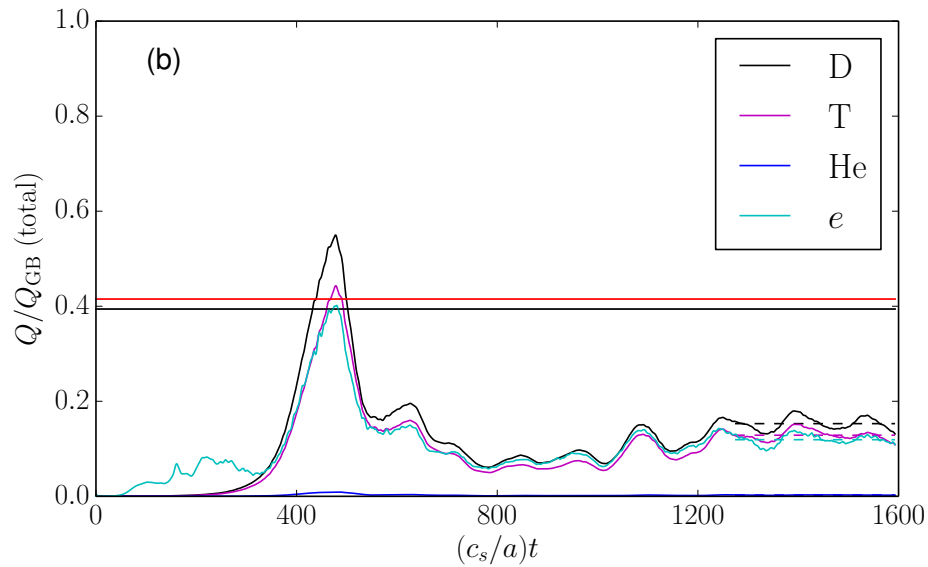


Figure 6: GYRO nonlinear simulation at  $r/a = 0.4$  with both  $a/L_{Ti}$  and  $a/L_{Te}$  increased by 10% above the baseline values in Table 3. Even with increased gradients the nonlinear simulation is zonal-flow dominated and produces negligible flux.

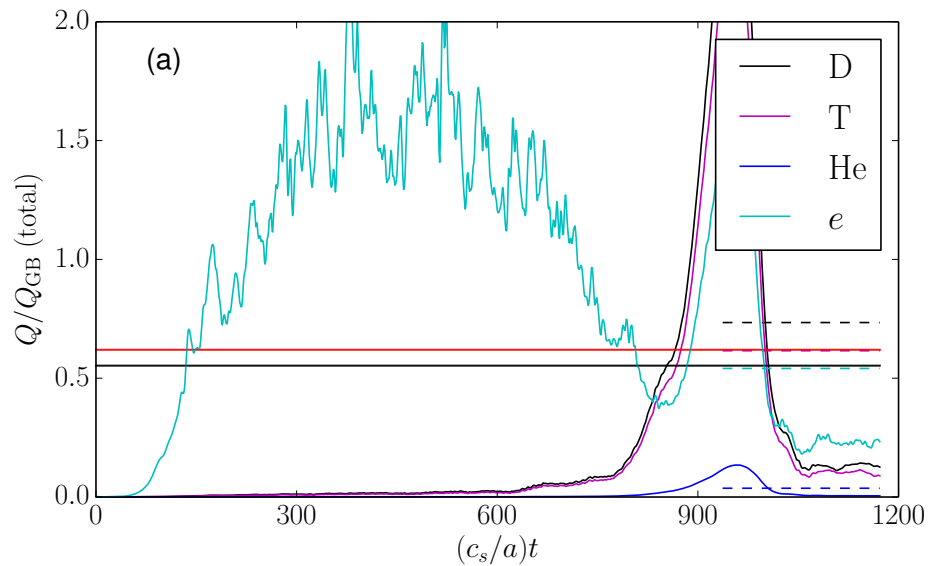


Figure 7: GYRO nonlinear simulation at  $r/a = 0.5$ . TGLF results for electron and ion fluxes are shown in red and black lines, respectively. Gradients are the nominal values shown in Table 3.

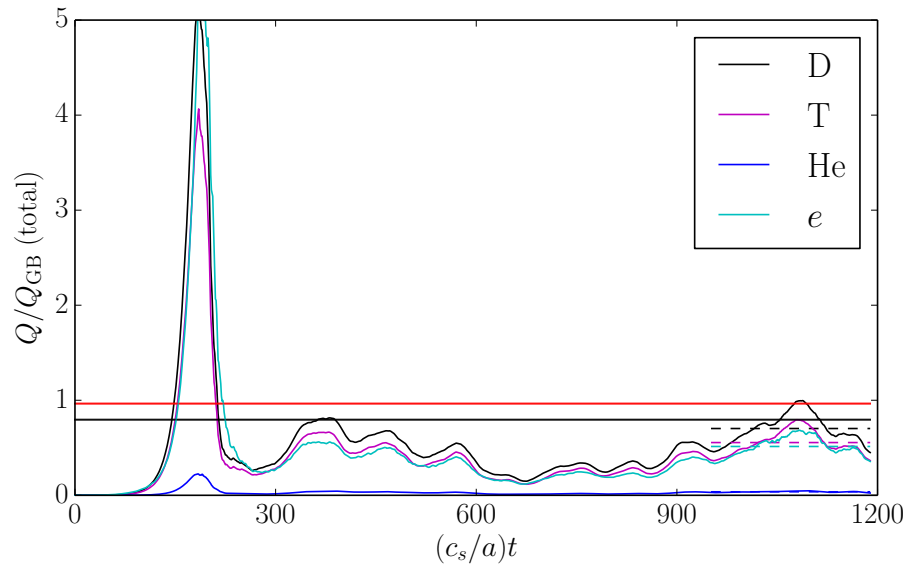


Figure 8: GYRO nonlinear simulation at  $r/a = 0.6$ . TGLF results for electron and ion fluxes are shown in red and black lines, respectively. Gradients are the nominal values shown in Table 3.

## 4 Nonlinear simulations for recalibration (Q2)

In this section we summarize nonlinear GYRO simulations carried out to serve as a database for TGLF recalibration. As specified in the milestones, these scans were electrostatic without impurities. However, we have improved slightly on the realism specified in the milestone by treating the Deuterium and Tritium as separate gyrokinetic species rather than lumping them into a single species. Many of the simulations fail to reach a clear steady-state, so tabulation of steady-state fluxes is not warranted in selected cases. In the figures that follow, we show the time-traces to give a clear indication of the relative reliability of the average value.

Simulations are carried out varying both the electron temperature gradient,  $a/L_{Te}$  and the ion gradient  $a/L_{Ti}$  (constant for both species). In the milestone,  $q$ -scans were specified. To this end, we carried out simulations for  $r/a = 0.4, 0.5, 0.6$ , noting that  $q$  increases monotonically as  $r$  increases. One important aspect of this strategy is that  $s$  is also increased in a self-consistent manner. Finally, in each case, gradients are divided into two groups: "weak gradients" and "strong gradients". The former cover the range very close to marginal stability, whereas the latter cover the range well above threshold where good steady-states of turbulence are expected. The simulation parameters for each radius are those given in Tables 1 and 2. In addition, we assume  $n_D = n_T = n_e/2$ . To automate the GYRO scans, we used the Integrated Plasma Simulator (IPS) framework. Also, note that in these results, the Tritium energy flux is consistently lower (by a small amount) than the Deuterium flux. This result was noticed by Estrada-Mila as early as 2005 [16]. The simulation results are summarized as a scatter plot in Fig. 9. We also show the time-traces of all simulations in Appendix A.

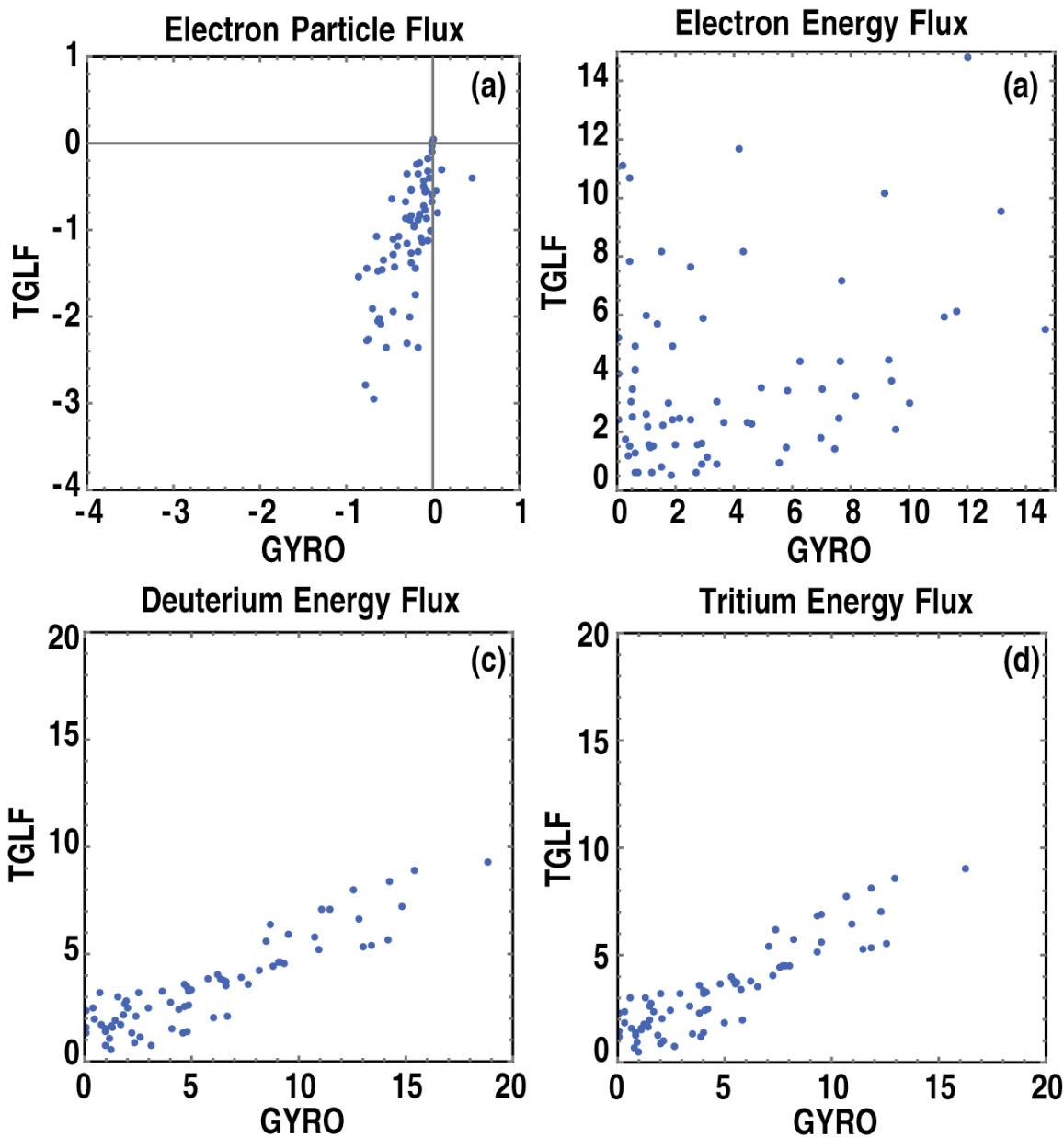


Figure 9: Comparison of the TGLF and GYRO (a) electron particle flux, (b) electron energy flux, (c) deuterium energy flux, and (d) tritium energy flux for the 72 ITER cases.

## 5 TGLF Recalibration

### 5.1 Comparison of TGLF with the 72 GYRO Q2 ITER Simulations

As part of the 2nd quarter milestone, and as summarized in the previous section, GYRO [1] simulation results for 72 scans around three different radii ( $r/a = 0.4, 0.5, 0.6$ ) of an ITER base case were presented. Scatter plots of the TGLF vs GYRO fluxes for these 72 GYRO Q2 runs are shown in Fig. 9. Because nearly all of the simulations are above the linear threshold, at first glance the results appear to indicate that GYRO predicts, on average, more transport than TGLF. While this is true of most of the simulation cases, it is not true of the cases very close to the GYRO threshold. Indeed, looking in the region close to the vertical (TGLF) axis, we see a cluster of points which are stable according to GYRO but nevertheless remain well above the stability threshold according to TGLF. This is the relatively small region of parameter space we are interested in. In addition to the difference near the GYRO marginal stability region, note also that the electron particle flux (Fig. 9a) from TGLF has a stronger pinch than GYRO, and the electron energy flux (Fig. 9b) from TGLF has an unusually large amount of scatter. Examination of these cases shows that this is partly due to a much stronger electron energy flux from TGLF when  $a/L_{T_e} > a/L_{T_i}$  near the threshold for  $a/L_{T_i}$ . Additional simulations (not shown) indicated that the TGLF fluxes are a better match to GYRO when the temperature gradients are equal. The deuterium (Fig. 9c) and tritium (Fig. 9d) energy fluxes are systematically on a lower slope for TGLF than for GYRO but do not show the same scatter as the electron energy flux. As expected [16], both TGLF and GYRO show that each hydrogenic ion species has about the same energy flux. Some additional analysis shows that the strong shaping ( $\kappa = 1.5$ ) in these runs appears to be the reason why the TGLF ion energy fluxes are suppressed compared to GYRO.

### 5.2 Equal-temperature, circular nonlinear GYRO Q3 Simulations

The critical realization, then, is that because of the relatively poor agreement of TGLF with GYRO even for high gradients, it is difficult to assess the role of the Dimits shift in the differences. In order to obtain better agreement between TGLF and GYRO at moderate gradient (above threshold but not far above) to allow us to focus on the Dimits shift at low gradient, equal-temperature-gradient scans with a few adjustments to the plasma conditions were made in Q3. The flux-surface shape was set to a Miller circle with zero Shafranov shift. A finite electron collision frequency was added based on the core value for ITER. A summary of the input plasma parameters (held fixed in the scans) is given in Table 4. Three species are included kinetically: electrons, 50% deuterium, and 50% tritium. The same spectrum of poloidal wavenumbers is used for TGLF as for the GYRO turbulence simulations. A python script was written to convert a GYRO input file (`input.gyro.gen`) to one for TGLF (`input.tglf`) to facilitate these runs. This python script (`tglf_input_gyro.py`) is now part of the GACODE release version.

Table 4: Fixed plasma parameters for Q3 equal-temperature, circular nonlinear simulations

Parameter	$r/a$	$R/a$	$(a/c_s)v_{ee}$	$T_i/T_e$	$q$	$s$	$a/L_n$
Value	0.4	3.2	0.015	1.0	1.2	0.6	0.44

### 5.3 The Dimits Shift Regime

The results of a temperature gradient scan about the reference case in Table 4 with equal temperatures for all species is shown in Fig. 10. Since the tritium energy flux is nearly the same as the deuterium energy flux for both TGLF and GYRO, we plot only the latter in Fig. 10c. Overall,

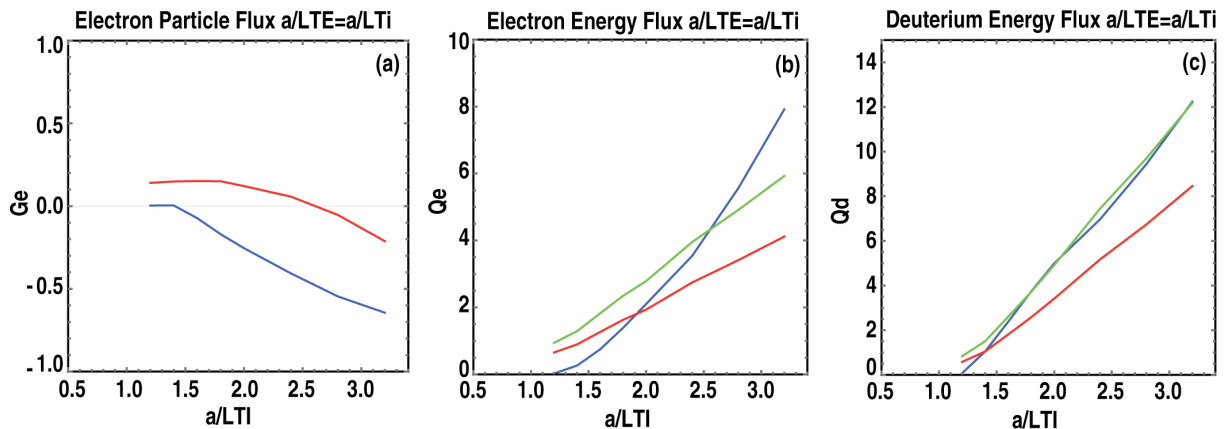


Figure 10: (a) Electron particle flux, (b) electron energy flux, (c) deuterium energy flux for GYRO (blue), TGLF (red) and 1.447 times TGLF (green) for the Q3 equal-temperature, circular case defined in Table 4.

the match of TGLF (red) to GYRO (blue) is not exceptional for the scan in Fig. 10. However, rescaling the TGLF deuterium energy flux by a factor of 1.447 to match the highest gradient GYRO point (green) gives a good fit to GYRO and clearly shows the drop in the GYRO flux near the linear threshold. The upshift of the critical gradient (Dimits shift) for the GYRO runs is not very large (approximately from  $a/L_T = 0.8$  to 1.4) even for this low- $q$  case. Rescaling the electron energy flux by the same 1.447 factor is not enough to match the slope of the GYRO flux. The GYRO electron energy flux is also more curved upward in shape than TGLF. The evolution of the RMS zonal ( $n = 0$ ) and finite toroidal mode number ( $n > 0$ ) electric potentials for the GYRO simulation for the lowest three temperature gradients is shown in Fig. 11. For the lowest gradient ( $a/L_T = 1.2$ ) in Fig. 11a, the zonal and finite- $n$  potential fluctuations have large oscillations but then settle into a zonal-flow-dominated state characteristic of the Dimits shift, or *flow-dominated*, regime. As the gradient is increased, the zonal and finite- $n$  electric potential fluctuations exchange dominance in the long-time-average state. The long-time average en-

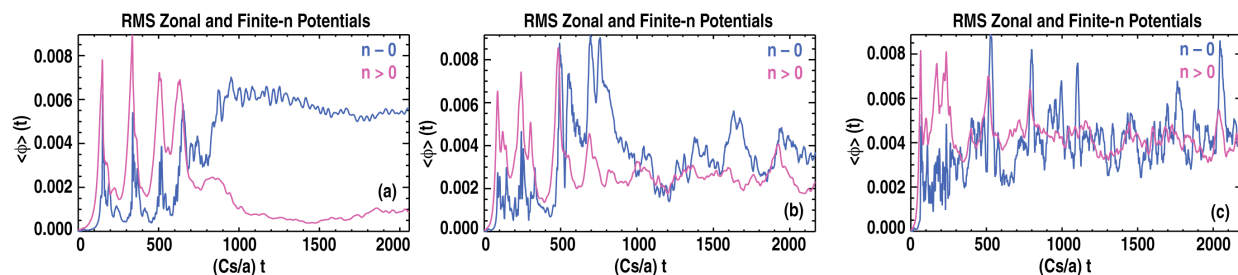


Figure 11: RMS zonal ( $n = 0$ ) and finite- $n$  ( $n > 0$ ) electric potential fluctuation amplitudes for (a)  $a/L_T = 1.2$ , (b) 1.4 and (c) 1.6. These time-traces are samples from the Q3 equal-temperature, circular case simulations.

ergy of the fluctuating electric field  $\langle \delta \mathbf{E} \cdot \delta \mathbf{E} \rangle$  in gyroBohm units for the zonal ( $E_0$ ) and finite- $n$  ( $E_1$ ) contributions is shown in Fig. 12. The latter figure clearly illustrates the rapid transition to the flow-dominated regime at low driving gradient.

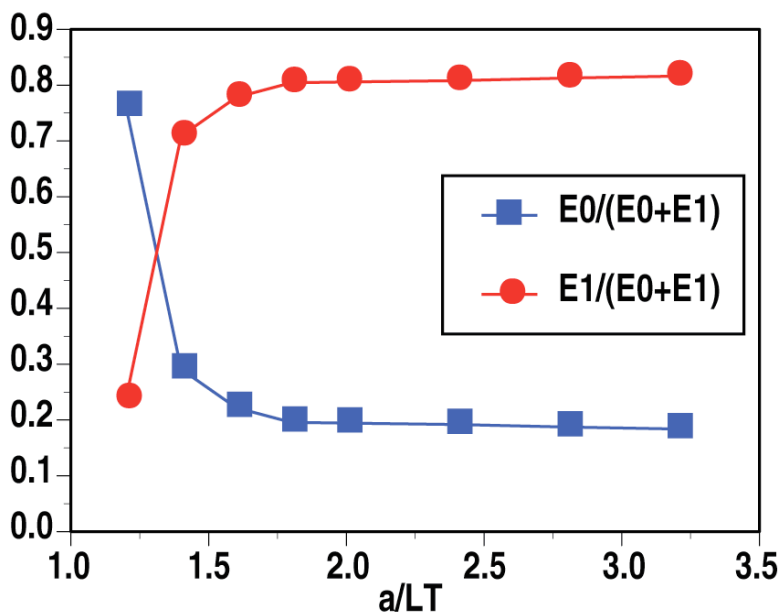


Figure 12: Fraction of long-time-average electric field energy for the zonal ( $E_0$ ) and finite- $n$  ( $E_1$ ) components for the GYRO Q3 simulations.

## 5.4 Initial recalibration attempt

To describe the transition effect illustrated in Fig. 12, an initial recalibration attempt was made in which an *ad hoc* model for the Dimits shift regime was constructed and applied to TGLF in order to fit GYRO [1] temperature gradient scans at two different magnetic shears. Different values of the fit parameter in the model were needed in order to fit each simulation. The potential impact of the Dimits shift on ITER fusion performance prediction was then tested using the strongest value for the fit parameter. A dramatic potential impact was found, motivating a deeper study of the physics behind the Dimits shift. The Dimits shift is known to be triggered by zonal (axisymmetric) electric field fluctuations. While zonal flows normally play a strong role in regulating turbulence, near the instability threshold they can become so large that they quench the ion-scale turbulence entirely. The original turbulence simulations by Dimits used the adiabatic electron approximation. With kinetic electrons, a complete quenching of the turbulence is not found but rather the turbulence is reduced to a low level. The TGLF saturation rule models the zonal flow damping represented by the curvature drift. The main impact in the saturation rule is a geometric mean of the linear growth rate and the curvature drift. This simple model does not capture the nonlinear upshift of the effective critical temperature gradient (Dimits shift) seen in the turbulence simulations.

As the overarching result of the 2015 Theory and Computation performance target, we will subsequently present a new model of the saturated turbulence intensity that captures well the role of zonal flows in saturating the turbulence at all scales from ion to electron. This new model is based on the properties of independent extreme-scale simulations of multiscale turbulence [17] performed by Howard *et al.* [6] with the GYRO code. The new model will be shown to simultaneously solve **two outstanding problems** with transport modeling. First, it captures the Dimits shift near marginality (the original motivation). Second, it describes the dependence of the high- $k$  transport on the low- $k$  turbulence that is observed in multiscale simulations. Both can have an impact on ITER performance. The Dimits shift improves the fusion performance, but the strong increase in electron energy transport, observed when the low- $k$  turbulence is weak, could potentially exert a negative influence on ITER performance. With the new model, we will assess the impact of both mechanisms on ITER fusion power predictions.

The results of the new model for ITER show that it is potentially **misleading** to simulate only the low- $k$  turbulence. The high- $k$  part of the fluctuation spectrum also contributes to ITER energy transport and requires much more comprehensive (and computationally expensive) multiscale simulation to determine the correct transport (and thus fusion performance) in ITER.

## 5.5 Multiscale impacts on ITER and final GYRO Q4 simulations

In ITER, the electron and ion energy fluxes (expressed in gyroBohm units) is small over a much larger region of the core plasma than in present day tokamaks. This is illustrated in Fig. 13. This weak energy flux means that a large fraction of the ITER minor radius is near the turbulence

threshold. Therefore, it is important to model the near-threshold region as accurately as possible. In Fig. 14, a new Q4 temperature gradient scan for an ITER-like case is shown. In this plot,

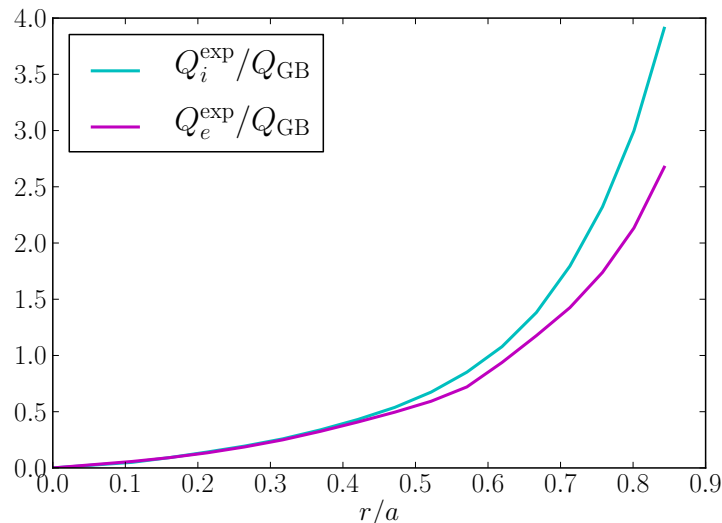


Figure 13: Power balance electron and ion energy fluxes in gyroBohm units for an ITER case.

the TGLF and GYRO electron and deuterium energy fluxes are compared. Three kinetic species are included: electrons, 50% deuterium, and 50% tritium. An important difference is that for the final Q4 simulations work we used significantly higher radial resolution (more gridpoints per gyroradius) than in previous simulations, as will be clarified shortly. The same spectrum of toroidal wavenumbers is used for TGLF as for the GYRO simulations. A clear up-shift of the effective critical gradient is seen in the GYRO fluxes compared to TGLF. Regarding the radial resolution, the GYRO simulations were found to be sensitive to the radial grid spacing (or equivalently, the maximum radial wavenumber resolved). The impact of repeating the GYRO scan done in the third quarter at higher radial resolution is shown in Fig. 15. The lowest resolution case,  $\Delta r/\rho_i = 0.56$  ( $k_{x,\text{max}} \sim 5.6$ ), is that shown in the Q3 report. In the present report we have repeated simulations at  $\Delta r/\rho_i = 0.37$  ( $k_{x,\text{max}} \sim 8.4$ ) and  $\Delta r/\rho_i = 0.28$  ( $k_{x,\text{max}} \sim 11.2$ ). We observe that the flux drops with increasing radial resolution, an effect consistent with the observation the under-resolution of the poloidal or radial directions gives rise to a small, spurious numerical flux. The effect of higher resolution has saturated for the lowest temperature gradients but there could be further drops at higher gradients. In general, the simulations for the lowest gradients have very long transients and/or intermittency and require very-long-time simulations to obtain good statistics. The highest toroidal wavenumbers ( $k_y$ ) are most impacted by the radial wavenumber ( $k_x$ ) maximum since  $k_{x,\text{max}}/k_y$  is smallest at high  $k_y$ . As the temperature gradient is increased the flux spectrum increases at higher  $k_y$  so higher radial resolution is required.

These GYRO simulations only include ion-scale low- $k_y$  wavenumbers. There is also a problem with the fidelity of TGLF to GYRO at high- $k_y$  wavenumbers where electron temperature gradi-

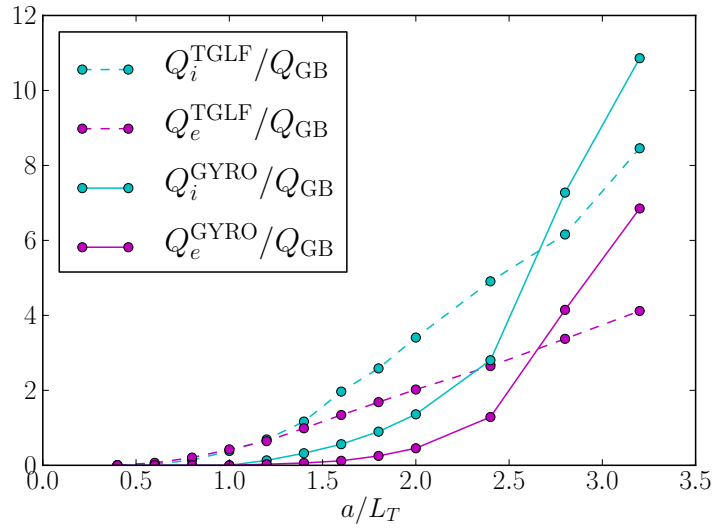


Figure 14: Q4 temperature gradient scan for an ITER-like case comparing GYRO and TGLF energy fluxes in gyroBohm units.

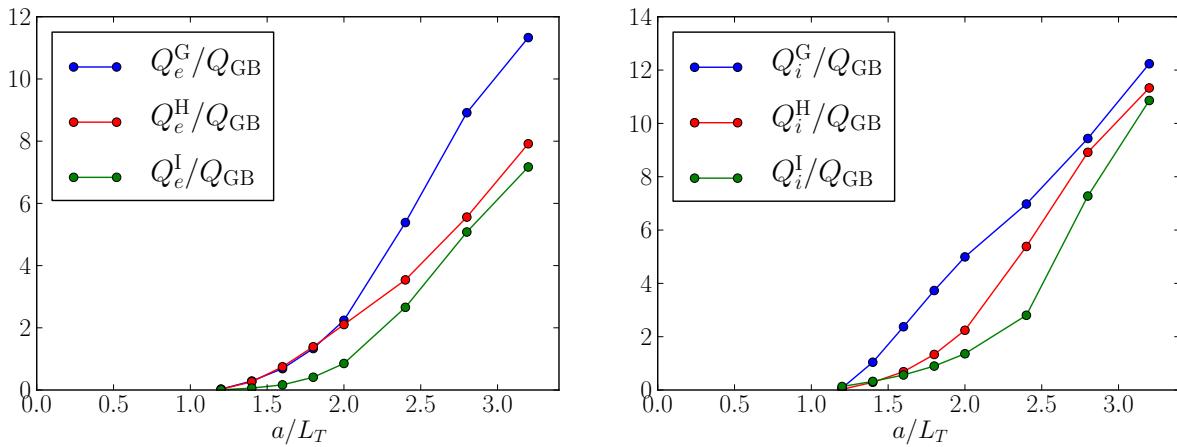


Figure 15: Convergence of the GYRO Q4 scan in Fig. 14 with radial wavenumber resolution. Cases G, H and I show simulations for  $k_{x,\max} \sim 5.6, 8.4,$  and  $11.2,$  respectively.

ent (ETG) instabilities exist. The most extreme example of this is in the high- $\beta_p$  regime. The electron temperature predicted by TGLF is far above the experimental temperature as shown in Fig. 16. It will be shown, that the electron energy transport can be due to ETG modes that are undamped by zonal flows because the low- $k$  turbulence is weak. Such an extreme electron energy flux enhancement over the TGLF prediction for ITER in the baseline H-mode regime is not seen in present tokamak experiments. However, understanding the physics of the multi-

scale interaction of ETG modes is a high priority so that the conditions under which the ETG enhancement occurs can be predicted with confidence.

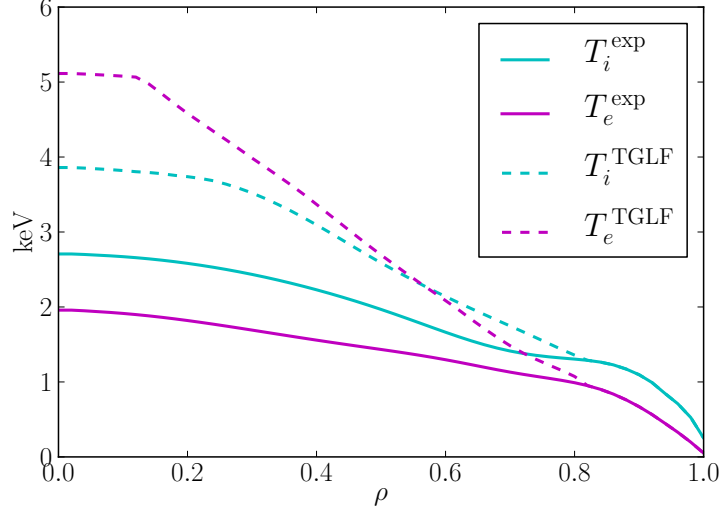


Figure 16: Ion and electron temperature profiles measured in a DIII-D high- $\beta_p$  discharge and predicted by TGLF.

## 5.6 Properties of the electric potential turbulence spectrum

It is well established that the quasilinear weights of the fluxes agree with the ratios of the turbulence driven fluxes (electron and ion energy, particle and momentum). These quasilinear weights need to be multiplied by a model of the electric potential fluctuation spectrum in order to compute the magnitude of the fluxes. In order to complete the quasilinear transport calculation in TGLF, the  $k_y$ -spectrum of the potential fluctuation intensity at the peak  $k_x$ -value is needed [18]. Accurately modeling the properties of the potential spectrum are the key to produce a more accurate quasilinear model. Fortunately, the nonlinear spectrum of the potential fluctuation has some simple properties that can be exploited in building a model. The time and flux surface average 2-D  $(k_x, k_y)$  spectrum of the electric potential intensity is well represented by a shifted Lorentzian shape in  $k_x$  [18]. Note that this  $k_x$  does not include the radial wavenumber contribution from the eikonal and is independent of magnetic shear. It is just the Fourier transform of the radial grid in GYRO. The peak of the spectrum in  $k_x$  at each  $k_y$  is at  $k_{x,\text{shift}} = \langle \phi^2 k_x \rangle / \langle \phi^2 \rangle$ . Here  $\langle f \rangle$  is a sum over the  $k_x$ -spectrum of  $d k_x f$  where  $d k_x$  is the spacing between wavenumbers. The width of the potential spectrum in  $k_x$  is

$$k_{x,\text{RMS}} = \sqrt{\frac{\langle \phi^2 (k_x - k_{x,\text{shift}})^2 \rangle}{\langle \phi^2 \rangle}}. \quad (1)$$

This width scales with  $k_y$  such that, at low  $k_y$  ( $k_y < 1$ ),  $k_y/k_{x,\text{RMS}}$  is nearly constant as illustrated in Fig. 17. Many low- $k_y$  cases have been examined, finding that the variation of  $k_y/k_{x,\text{RMS}}$  from a constant is weak except at the lowest  $k_y$  where it goes to zero. Defining an effective nonlin-

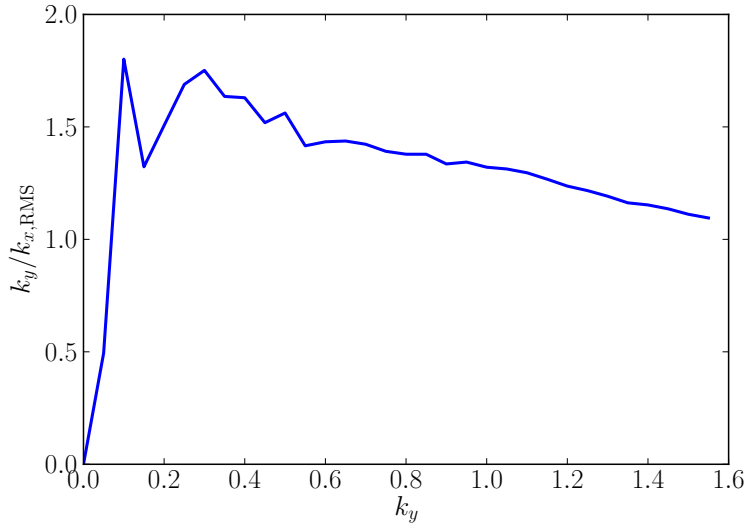


Figure 17:  $k_y/k_{x,\text{RMS}}$  for the GA-STD case parameters.

ear growth rate by  $\gamma_{\text{eff}} = k_{x,\text{RMS}}k_y\phi(k_{x,\text{shift}}, k_y)$  it is found that the linear growth rate has more variation with  $k_y$  than this effective growth rate. This is illustrated in Fig. 18. Examining many cases, the common property of the effective growth rate is that it rises from zero at  $k_y = 0$  more quickly than the linear growth rate and is relatively flat compared to the linear growth rate for  $k_y$  greater than some value. We will come back to these properties of the low- $k$  potential spectrum shortly, but now let us examine the high- $k$  properties. Extremely computing-intensive GYRO simulations with both ions and electrons with the physical mass ratio have been performed for C-Mod L-Mode edge region discharges [6]. In Fig. 19, we plotted the TGLF and GYRO electron and deuterium energy fluxes for three multiscale GYRO simulations that scan the ion temperature gradient at fixed electron temperature gradient. The TGLF deuterium energy flux is a reasonable match to GYRO, but the electron energy flux is too high at high ion temperature gradient because the high- $k$  ( $k_y > 1$ ) contribution is too large. The nonlinear saturation rule in TGLF for the high- $k$  ETG modes was fit to a single multiscale GYRO simulations of the GA-STD case with a reduced electron mass [17]. The TGLF high- $k$  electron energy flux does not capture the coupling of the high- $k$  transport to the low- $k$  turbulence driven by the ion temperature gradient. It is clear from the multiscale GYRO simulations that the ETG high- $k$  contribution is suppressed by an increase in the ion temperature gradient. In Fig. 20 we plot the effective nonlinear growth rate and the linear growth rate vs  $k_y$  for the multiscale simulation at the highest ion temperature gradient. The linear growth rate far exceeds the effective growth rate at high  $k$ . The effective growth rate is limited to approximately the same value at high  $k$  as it has for the low- $k$  sector for this case. The nonlinear saturation of the electric potential produces this

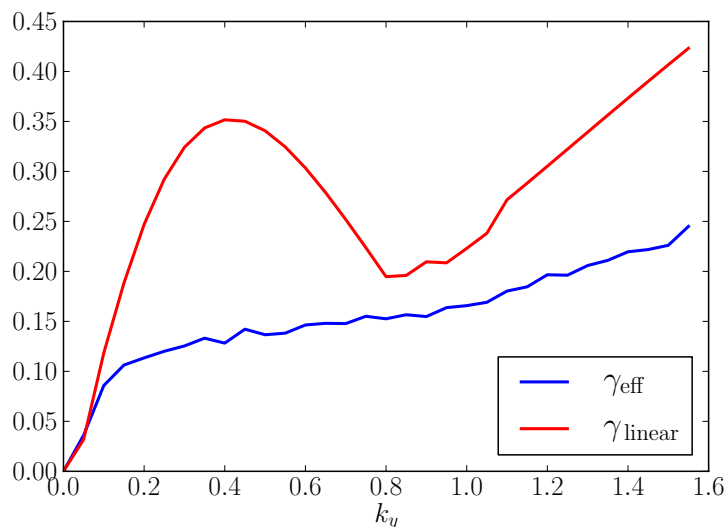


Figure 18: Linear growth rate spectrum (red) compared to the effective non-linear "growth rate" determined from the saturated potential spectrum (blue)

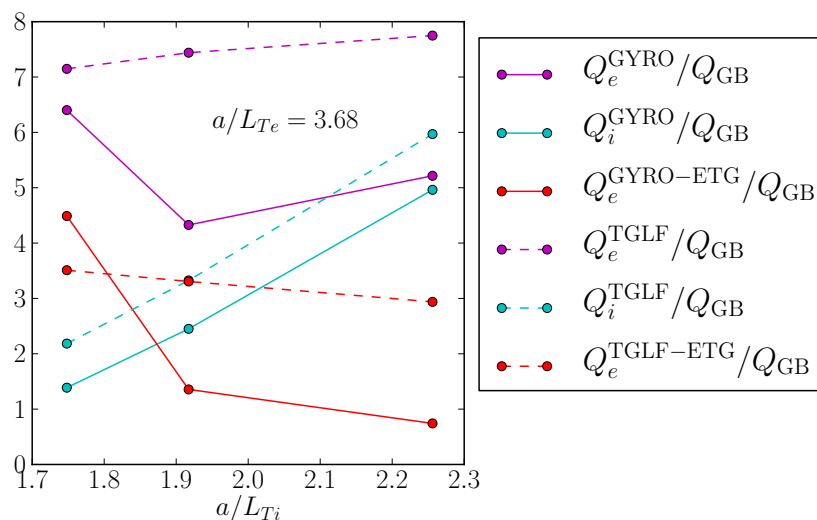


Figure 19: GYRO and TGLF-SAT0 electron, ion and high- $k_y$  electron energy fluxes for three of the multiscale cases of Howard [6].

flat effective growth rate spectrum. What can compete with the large high- $k$  linear growth rate? The answer can be seen in the nonlinear time derivative including the fluctuating  $\mathbf{E} \times \mathbf{B}$  convection. The Fourier transform in  $k_x, k_y$  of the convective derivative for the fluctuating distribution

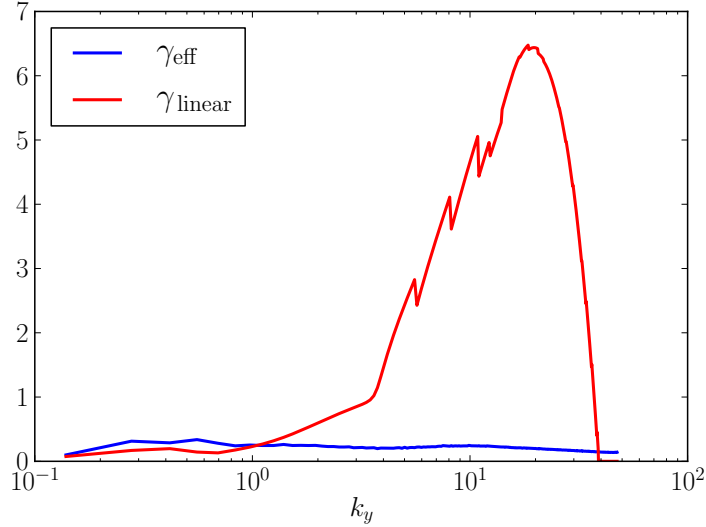


Figure 20:  $\gamma_{\text{eff}}$  and  $\gamma_{\text{linear}}$  vs  $k_y$  for the GA-STD case.

function  $f(k_x, k_y)$  can be written symbolically as

$$\frac{\partial f(k_x, k_y)}{\partial t} = \gamma_{\text{linear}}(k_y)f + k_y [k_x \phi(k_x, 0)] * f + [k_y k_x \phi(k_x, k_y)] * f, \quad (2)$$

where  $*$  denotes a convolution. The first term is the linear growth. The second term is the  $\mathbf{E} \times \mathbf{B}$  convection from the fluctuating zonal ( $k_y = 0$ ) electric field. The third term is the convection from the finite  $k_y$  fluctuating electric field. We have seen in Fig. 20 that the linear growth rate far exceeds the effective nonlinear growth rate. The peak value of the third term in Eq. (2),  $k_x k_y \phi(k_x, k_y)$ , is bounded by the effective growth rate so it is not able to compete with the linear growth rate at high  $k_y$ . The zonal electric field spectrum  $k_x \phi(k_x, 0)$  (which is also the normalized  $\mathbf{E} \times \mathbf{B}$  velocity or zonal flow) has the same value independent of  $k_y$ . However the effective decorrelation rate of these zonal flows  $k_y k_x \phi(k_x, 0)$  increases with the  $k_y$  of the distribution function  $f$ . The strength of the zonal radial electric field ( $\mathbf{E} \times \mathbf{B}$  velocity in these normalized units) must compete with  $\gamma_{\text{linear}}/k_y$ . Since the strength of the zonal electric field is independent of  $k_y$  it should be balanced by the peak in  $\gamma_{\text{linear}}/k_y$ . The spectrum of the zonal radial electric field is basically Lorentzian in shape but has spikes at single values of  $k_x$ , so the local peak value may not be the best measure of the strength. We define the strength of the zonal electric field as  $E_x = \sqrt{\langle \phi(k_x, 0)^2 |k_x| \rangle}$ . For a Lorentzian-shaped spectrum  $\phi(k_x, 0) = \phi(0, 0) / [1 + (a_0 k_x)^2]$ , this gives  $E_x = \phi(0, 0)/a_0$  and  $\max[k_x \phi(k_x, 0)] = 0.5 E_x$ . This strength is about equal to the low- $k$  peak of  $\gamma_{\text{linear}}/k_y$  for 24 diverse GYRO simulations as shown in Fig. 21, including 4 of the new multiscale simulations and the 4 low- $k$  simulations of the same cases, the 8 GYRO simulations of Fig. 14 and 8 other high- $k_x$  resolution GYRO simulations varying parameters about the GA-STD case. The low- $k$  peak of  $\gamma_{\text{linear}}/k_y$  is the relevant one since the peak of the finite- $k_y$  drive

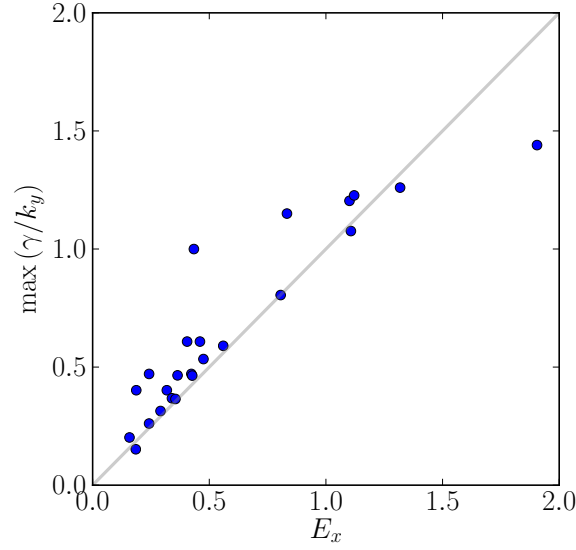


Figure 21:  $E_x$  and  $\gamma_{\max}/k_{y,\max}$  for 18 GYRO simulations.

term for the zonal distribution function in Eq. (3) peaks at low  $k_y$ .

$$\frac{\partial f(k_x, 0)}{\partial t} = \frac{ik_x}{R} \omega_d + [k_y k_x \phi(k_x, k_y)] * f(k_x, k_y). \quad (3)$$

The properties of the nonlinear potential spectrum can be modeled with a simple formula. If  $k_{y,\max}$  is the value of  $k_y$  at which  $\gamma_{\text{linear}}/k_y$  is maximum for  $k_y < 1$  and if  $\gamma_{\max}$  is the value of  $\gamma_{\text{linear}}$  at  $k_{y,\max}$ , then the strength of the zonal electric field is modeled by

$$E_x = \alpha_{\text{ZF}} \gamma_{\max} / k_{y,\max} \quad (4)$$

The effective nonlinear growth rate is modeled by

$$\gamma_{\text{modell}} = \begin{cases} cz_2 k_{y,\max} E_x + \max[\gamma_{\text{linear}} - cz_2 k_y E_x, 0] & k_y > k_{y,\max} \\ \max[\gamma_{\text{linear}} - cz_1 E_x (k_{y,\max} - k_y), 0] & k_y \leq k_{y,\max} \end{cases}. \quad (5)$$

The zonal flow damping of the mode at  $k_{y,\max}$  is zero for the models since this mode exactly matches the zonal flow decorrelation rate. The modell formula for  $k_y \leq k_{y,\max}$  can be written in the form

$$\gamma_{\text{modell}} = \max[(-cz_1) k_{y,\max} E_x + \gamma_{\text{linear}} - (-cz_1) k_y E_x, 0], \quad (6)$$

which shows its close relation to the  $k_y > k_{y,\max}$  formula ( $cz_1 = -cz_2$ ). For  $k_y < k_{y,\max}$ , the nonlinear  $\gamma_{\text{eff}}$  spectrum is observed to drop to zero faster than the linear growth rate in general. The coefficient  $cz_1 = 0.48$  is determined by minimizing the error for 83 low- $k$  GYRO simulations that were used to determine the original TGLF saturation model. If the zonal flow damping was not

needed, this parameter would not improve the fit. The coefficient  $cz_2 = 1.0$  is determined by approximately fitting to the multiscale GYRO simulation with the largest electron energy flux. The formula for  $k_y > k_{y,\max}$  gives a flat effective growth rate if the linear growth rate is less than  $cz_2$  times the zonal flow decorrelation rate  $k_y E_x$  which agrees with the high-ion-temperature-gradient multiscale simulation in Fig. 20. If the high- $k$  linear growth rate exceeds the zonal flow decorrelation rate then the effective growth rate can increase above  $\gamma_{\max}$ . This is what happens in the lower ion-temperature-gradient multiscale simulations. In Fig. 22 are shown the effective growth rate and the model1 (red) versus  $k_y$  for the same multiscale simulations as in Fig. 19. The highest ion-temperature-gradient case (Fig. 22a) has a low- $k$  peak in  $\gamma_{\text{linear}}/k_y$  that is also a global maximum so the model gives a flat growth rate spectrum that matches the GYRO result. As the ion temperature gradient is lowered (Figs. 22b,c) at fixed electron temperature gradient, a second high- $k$  peak in  $\gamma_{\text{linear}}/k_y$  becomes the global maximum which exceeds the strength of the zonal electric field. The model well-matches the location in  $k_y$  and magnitude of the bump in the effective growth rate spectrum as the ion temperature gradient, and hence the strength of the zonal electric field, is lowered (Figs. 22 b,c). The model1 does not match the smoothing of the the bump in  $k_y$  which is due to the third term in the convective derivative ( $k_y - k_y$  coupling). This effect can be included by making a weighted average of the model1 growth rates. This  $k_y$ -mixing version of the effective model2 growth rate is shown in Fig. 22 as the green curves. The width of the weight function (2.0) was chosen to fit the GYRO spectrum for the highest peak case. The coefficient  $cz_2$  needed to be lowered to  $cz_2 = 0.92$  in order for model2 to fit the spectrum.

$$\gamma_{\text{model2}} = \begin{cases} \int_{k'_y > k_{y,\max}} \gamma_{\text{model1}}(k'_y) W(k_y, k'_y) / W_{\text{norm}} & k_y > k_{y,\max} \\ \gamma_{\text{model1}} & k_y \leq k_{y,\max} \end{cases} \quad (7)$$

where

$$W(k_y, k'_y) = \frac{k_y^2}{1 + 2.0(k_y - k'_y)^2} \quad W_{\text{norm}} = \int_{k'_y > k_{y,\max}} W \quad (8)$$

There is an overall normalization coefficient for the potential intensity model that is determined by minimizing the offset between the GYRO and TGLF effective energy diffusivities. All 83 of the Miller geometry cases are shown in Fig. 23. The statistical error between TGLF and GYRO for the new model (17% for  $Q_i$  and 22% for  $Q_e$ ) is very close to the original TGLF model for this data set [8]. The statistics for the particle flux are not used to determine the fit since the particle flux is near zero for most cases and changes sign. Nevertheless, the particle diffusivities in Fig. 23b are close to the equality line with GYRO demonstrating the viability of the quasilinear particle flux weights. Before testing the new model there is one more feature of the multiscale simulations that needs to be considered. Unlike the low- $k$  GYRO simulations the multiscale simulations have a radial wavenumber width that is not proportional to  $k_y$  but rather to  $\sqrt{k_y}$  at high  $k_y$ . This is shown in Fig. 24 where  $k_y/k_{x,\text{RMS}}$  vs  $k_y$  is plotted. The time average for the multiscale simulations is sufficient for high  $k$  but is not long enough to average out all of the low- $k$  fluctuations so, at low- $k$ ,  $k_y/k_{x,\text{RMS}}$  will be modeled by a constant as found for low- $k$

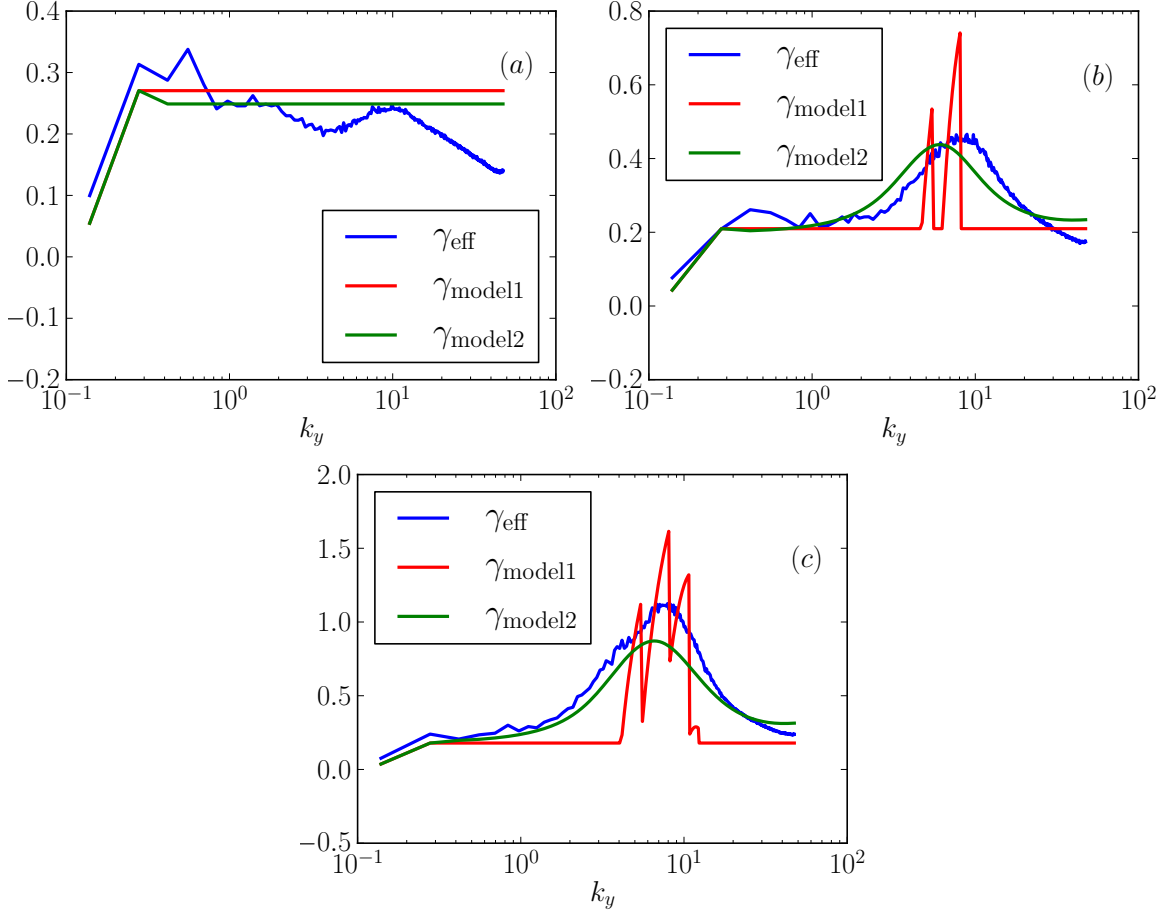


Figure 22:  $\gamma_{\text{eff}}$  (blue),  $\gamma_{\text{model1}}$  (red) and  $\gamma_{\text{model2}}$  (green) vs  $k_y$  for three multiscale simulations.

simulations. The model for  $k_{x,\text{RMS}}$  is

$$k_{x,\text{model}} = \begin{cases} c_x k_y & k_y < k_{y,\text{ETG}} \\ c_x k_y \sqrt{k_{y,\text{ETG}}/k_y} & k_y \geq k_{y,\text{ETG}} \end{cases} \quad (9)$$

A value of  $k_{y,\text{ETG}} = 2.2$  is determined by fitting the electron energy flux for the lowest ion temperature gradient multiscale simulation but you can see this value gives a reasonable fit to  $k_y/k_{x,\text{RMS}}$  as shown in Fig. 24. Putting these models together, the new multiscale saturation rule for TGLF-SAT1 is given by  $\phi_{\text{model}} = c_{\text{norm}} \gamma_{\text{model2}} / (k_{x,\text{model}} k_y)$ . The constant  $c_x$  can be absorbed into  $c_{\text{norm}}$ . The value of  $c_x = 1/\sqrt{0.56}$  is important for the spectral shift model of the equilibrium  $\mathbf{E} \times \mathbf{B}$  shear impact but that is not yet been integrated with the new model. Instead, the Waltz quench rule will be used to reduce the linear growth rates by the equilibrium  $\mathbf{E} \times \mathbf{B}$  shear before computing the new model potential. Applying the new model the to multiscale simulations, a very good agreement for all cases is found as shown in Fig. 25. The fit to highest

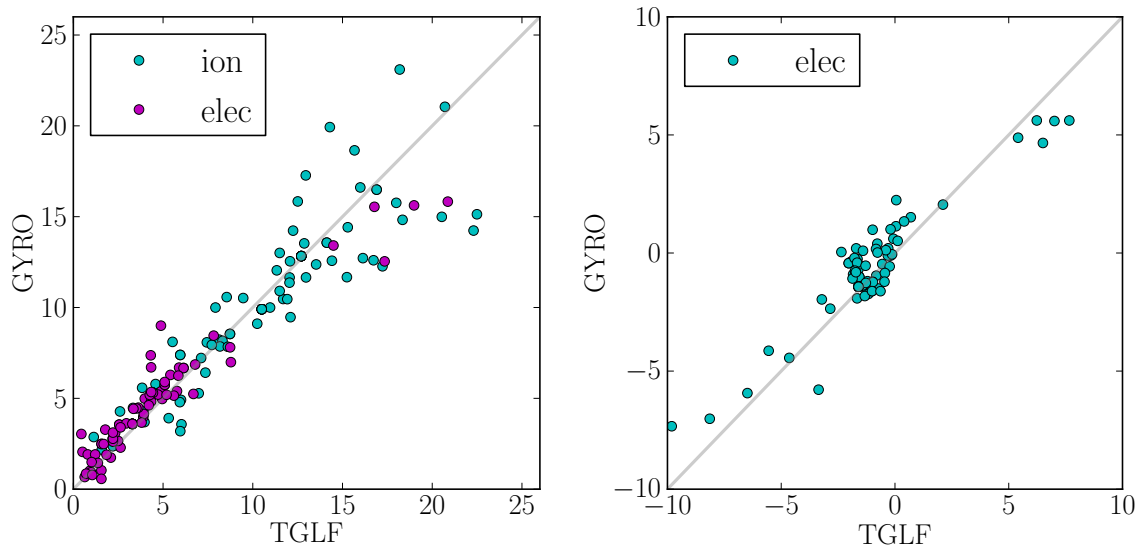


Figure 23: Fit of TGLF-SAT1 to GYRO for 83 low- $k$  Miller geometry cases. Energy fluxes are shown on the left and particle fluxes on the right.

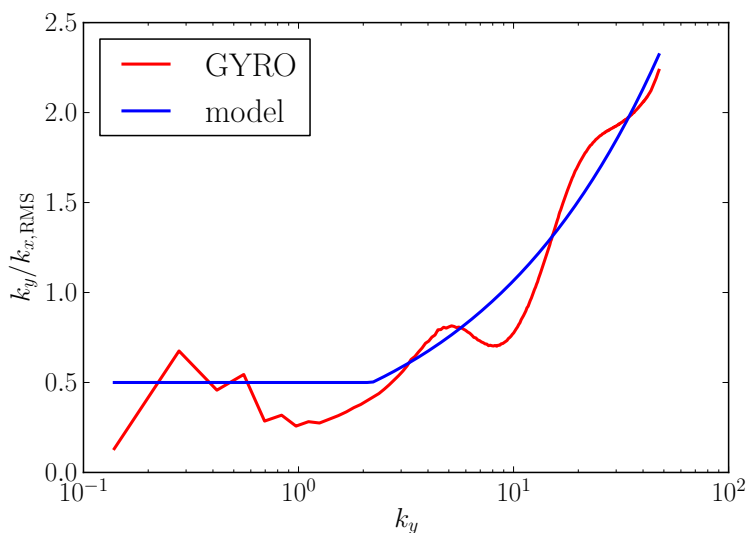


Figure 24:  $k_y/k_{x,RMS}$  vs  $k_y$  for SIM3.

electron energy flux value was tuned by the model fit  $k_{y,ETG} = 2.2$  but all of the other fluxes and cases are were not adjusted. The excellent agreement with the ion energy flux shows that the quasilinear ratio of electron to ion energy flux is accurate even when a large part of the electron energy flux is coming from the high- $k$  modes. The high- $k$  portion of the electron energy flux is

shown in Fig. 25 and the model reproduces the correct high- $k$  flux. The agreement is good for both variation in the ion temperature gradient (Fig. 25a) and the electron temperature gradient (Fig. 25b). In applying the new model to predicting the temperatures for the high- $\beta_p$  discharge,

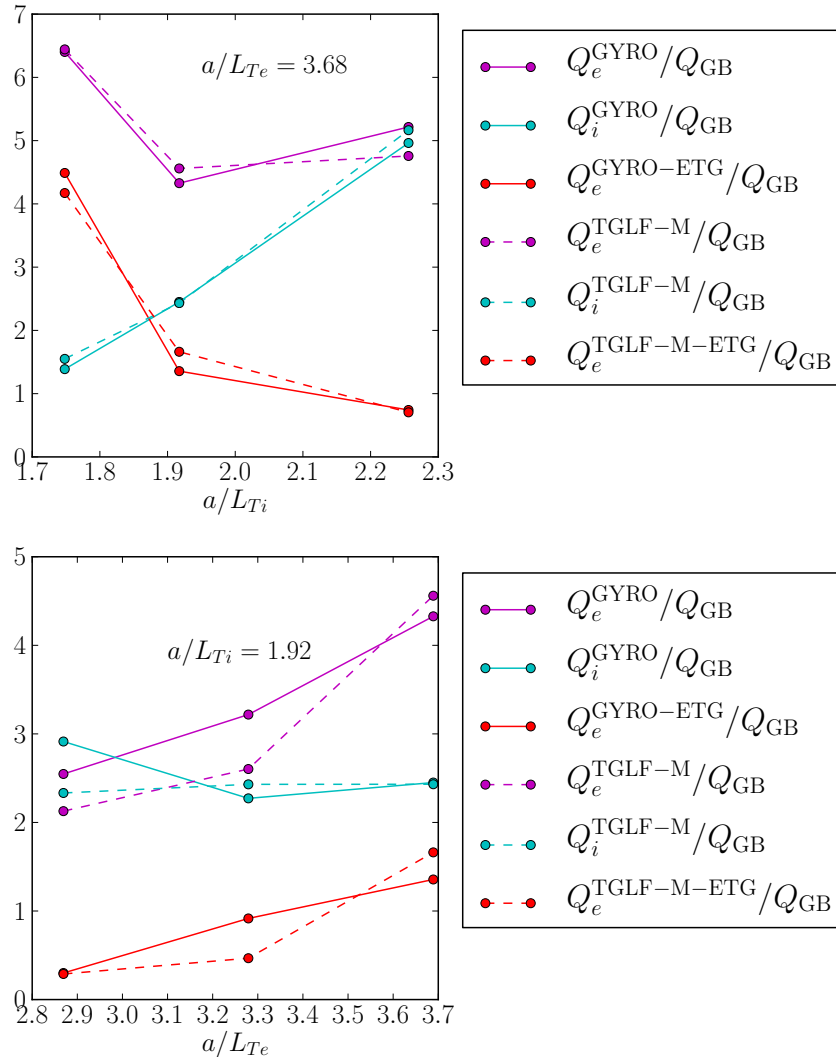


Figure 25: GYRO and TGLF-SAT1 fluxes for the multiscale simulations.

a significant improvement is obtained as shown in Fig. 26. In addition, the density and  $\mathbf{E} \times \mathbf{B}$  toroidal velocity has also been predicted in good agreement with the measurements. Very little particle or momentum transport was predicted by the original TGLF. For this discharge, the neoclassical ion energy transport is dominant due to the high safety factor. The ion temperature gradient is near the threshold for the ITG mode so the low- $k$  peak of  $\gamma_{\text{linear}}/k_y$  is small or zero. The damping of the high- $k$  modes due to zonal flows is small, allowing the high- $k$  ETG modes to become very large. The multiscale model lets the effective growth rate rise to the lin-

ear growth rate when there are no zonal flows which is a very large increase (see Fig. 24). The  $k_y$ -scaling of the radial wavenumber width  $k_{x,\text{RMS}}$  is also favorable to increasing ETG transport. The electron temperature profile is still predicted to be above the measurement. Reducing the zonal flow decorrelation of the high- $k$  modes ( $czf_2$ ) can bring the predicted electron temperature into agreement with the data. Multiscale simulations of this type of high- $\beta_p$  discharges are needed in order to see if ETG modes do indeed explain the electron energy transport. Although

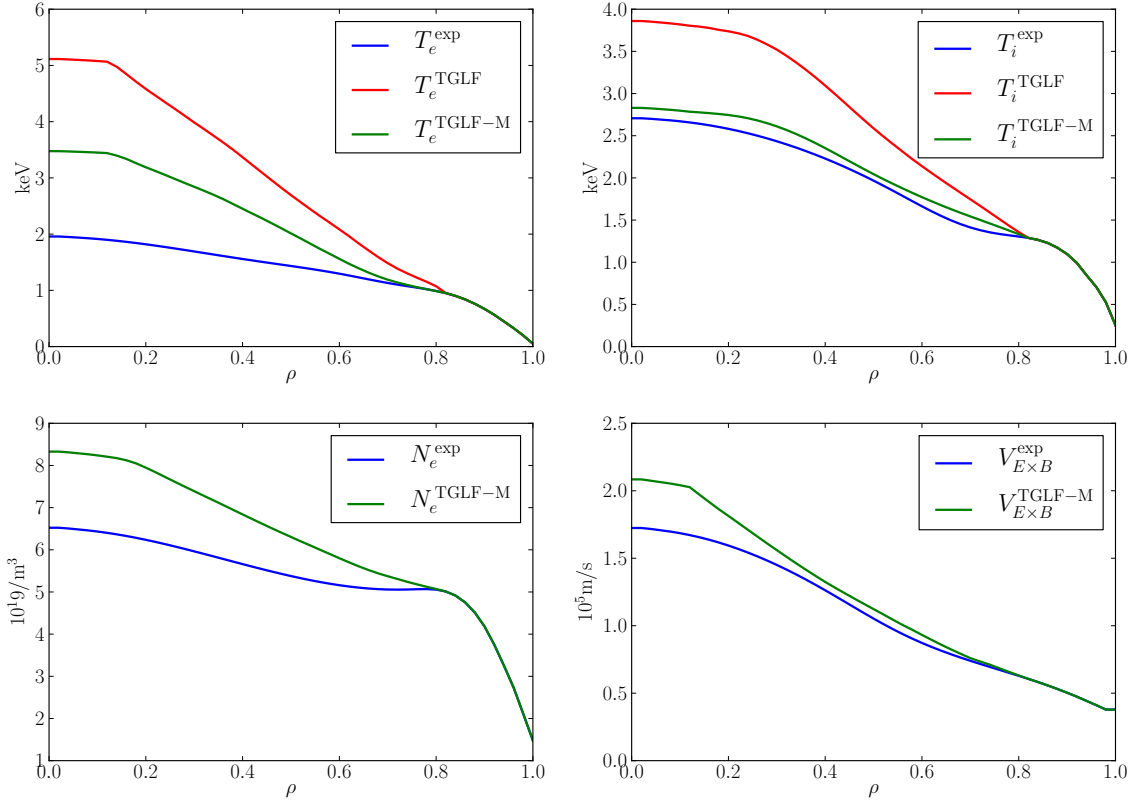


Figure 26: New TGLF-SAT1 predictions for the electron (a) and ion (b) temperatures, and for the electron density (c) and  $\mathbf{E} \times \mathbf{B}$  toroidal velocity (d) for the high- $\beta_p$  case of Fig. 24.

the new model has not explicitly tried to improve the fit to the GYRO scan of Fig. 14, the fit is greatly improved as shown in Fig. 27. Even the nonlinear upshift of the effective critical gradient is captured by the new model. This remarkable result is due to two effects. First, the new model has fluxes that are quadratic in the linear growth rate as the threshold is approached. The original TGLF saturation model had a linear dependence on the growth rate near threshold. Second, the zonal flow decorrelation model makes the model low- $k_y$  potential spectrum narrower, which accelerates the drop in the fluxes as the threshold gradient is approached from above.

The new model of zonal flow saturation of the turbulence has improved the fit of TGLF-SAT1 to

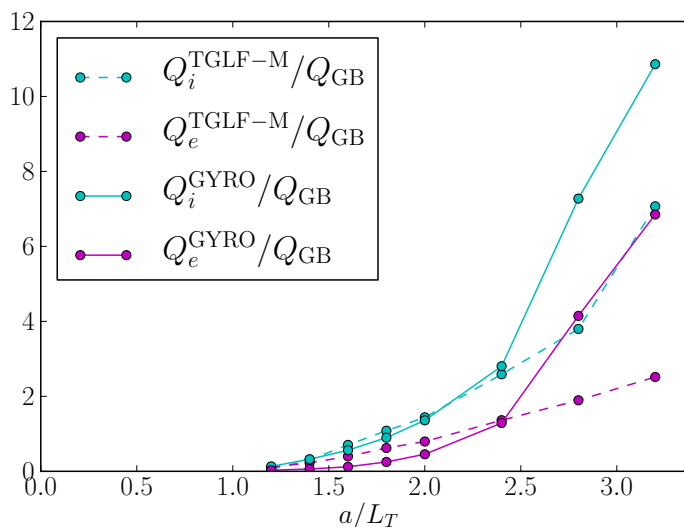


Figure 27: Multiscale TGLF-SAT1 predictions for the electron and ion energy fluxes compared to GYRO for the scan of Fig. 14.

GYRO at both extremes of the  $k_y$ -spectrum. The new TGLF-SAT1 is able to model the explosive growth of ETG modes when the low- $k$  turbulence is weak so that zonal flows are also weak. This effect, seen in the multiscale simulations, could have a negative impact on ITER predictions since the turbulence is weakly driven over much of the ITER core. The new model is also able to capture the near threshold upshift of the critical temperature gradient due which is due in part to zonal flows. This upshift was shown in the last quarter report to potentially yield a large improvement in ITER fusion power. Now that both of these effects are well modeled by TGLF-SAT1 we can find out which one influences the predicted ITER performance.

## 5.7 ITER Profile Prediction

The predicted electron and ion temperature and density profiles for an ITER case **ref Budny** are shown in Fig. 28 for both the original TGLF and TGLF-SAT1 with the new multiscale zonal flow saturation model.

The net impact of the new model is a 19% increase in the predicted fusion power for ITER (465 MW for TGLF versus 555 MW for TGLF-SAT1) at fixed pedestal pressure. Since the fusion power production increased for the new model the positive impact of the Dimits shift wins over the potentially large ETG energy transport. If the high- $k$  contribution to the TGLF-SAT1 fluxes are eliminated by including only low- $k$  modes, the gain in the fusion power compared to the original TGLF is even larger 44% (470 MW for TGLF versus 676 MW for TGLF-SAT1). Hence, ETG modes are predicted to have a non-negligible impact on electron transport in ITER. One im-

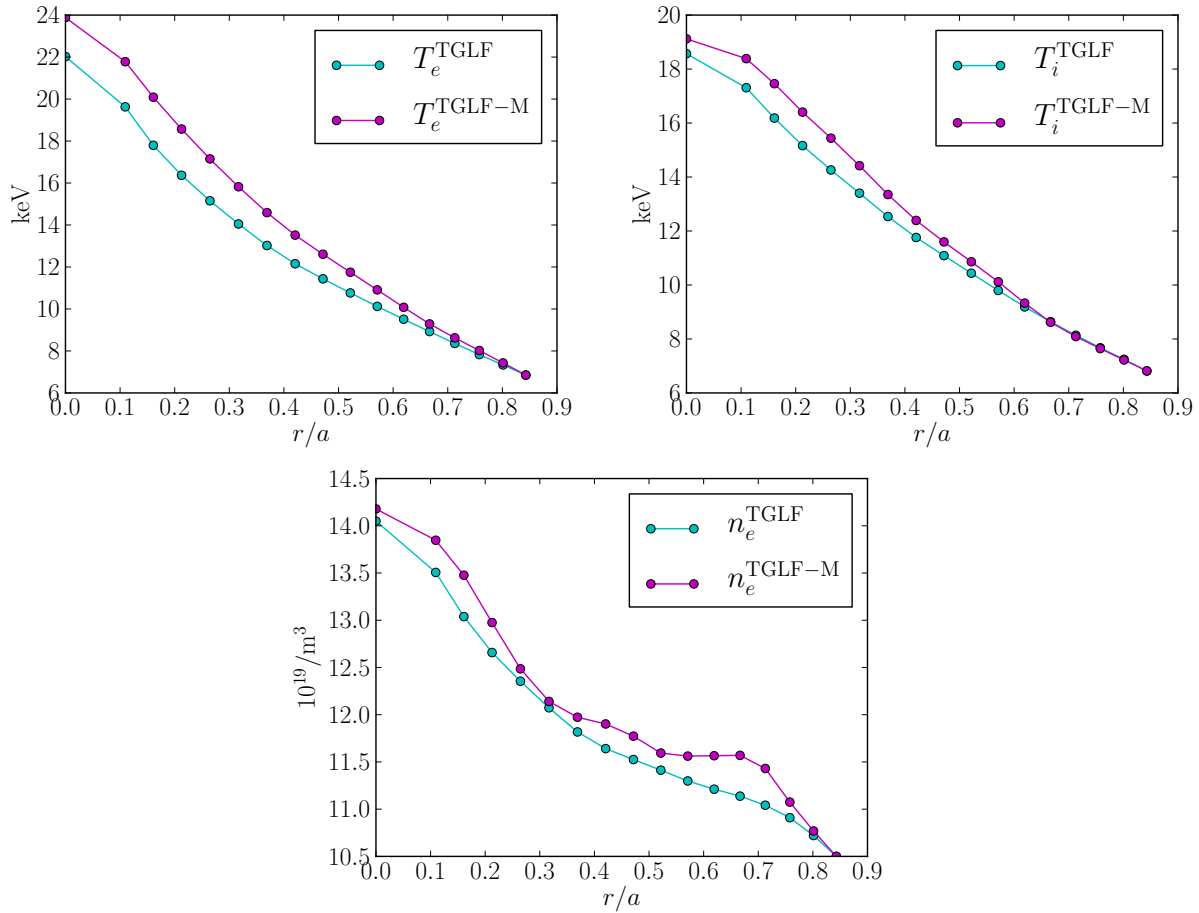


Figure 28: Predictions of a) electron temperature, b) ion temperature and c) electron density from TGLF and the new multiscale TGLF-SAT1 for an ITER case with 50% D-T + helium.

important fact about ITER that contributes to the net positive outcome is that the neoclassical ion thermal transport is small compared to the turbulent transport from the magnetic axis to the pedestal. In present tokamaks this is not the case. There is typically a region near the magnetic axis where ion neoclassical thermal transport is large enough to remove the power at an ion temperature gradient below the ITG mode threshold. This stable low- $k$  turbulence condition is just what is needed reduce the zonal flow decorrelation of the high- $k$  ETG turbulence, allowing it to become large. This does not happen in this ITER case because the low- $k$  turbulence is active all the way to the magnetic axis. The energy flux in ITER is also low in gyroBohm units as shown in Fig. 13. This means that the temperature gradients are close to stability threshold over much of the core. Therefore, even if there was no low- $k$  turbulence, the electron temperature gradient threshold for ETG modes would not be greatly exceeded. The presence of the active low- $k$  turbulence produces a nonlinear upshift in the effective critical electron temperature gradient for ETG modes through the zonal flow decorrelation.

## 6 Discussion

Two conditions where the TGLF quasilinear model failed to agree with nonlinear GYRO turbulence simulations were resolved. The first was in the flow-dominated, near-threshold regime, and the second was for the electron transport in the high- $k$  range of multiscale simulations. The impact of these effects on the fusion performance of ITER was investigated by developing a better model for the way zonal flows saturate the turbulence. The new zonal flow saturation model is conceptually very simple. Zonal flows are driven by low- $k$  turbulence to a strength where they are able to saturate all of the low- $k$  modes, thus distributing the turbulence spectrum in  $k_x$ -space in a self-similar way for each  $k_y$ . This results in a Lorentzian shaped  $k_x$ -spectrum with a saturated *effective growth rate* that is nearly the same for all  $k_y$  modes above the peak in  $k_y$ . The zonal flow saturation is effective even at high- $k_y$ , where the linear growth rate is far in excess of the effective growth rate but *not* in excess of the zonal flow decorrelation rate,  $k_y E_x$ . High- $k$  modes, that have growth rates above the zonal flow decorrelation rate, can saturate at a higher amplitude. This gives rise to a potentially large increase in the ETG transport, a phenomenon observed in multiscale GYRO simulations. This reinforces the observation that it is not possible to determine the ETG transport without simultaneous (i.e., multiscale) simulation of the ion-scale turbulence. The zonal flows provide the nonlocal coupling between the low- $k$  and high- $k$  turbulence. Fortunately, the proximity to the temperature gradient threshold, and the low neoclassical transport in ITER, conspire to suppress the ETG transport. In the end, the improved representation of the GYRO fluxes near threshold given by the new zonal flow saturation model in TGLF results in a 19% increase in the predicted ITER fusion power at fixed pedestal pressure for the present test case. Nevertheless, ongoing calibration, using low- $k$  as well as multiscale simulation, of the new TGLF-SAT1 saturation model with data is required.

### 6.1 Final Calibration Check via GYRO Comparisons

Using the recalibrated TGLF (TGLF-SAT1), we recomputed the ITER temperature and density profiles using TGYRO, and subsequently used this as a new baseline for comparison with GYRO. In this final comparison case we used TGLF with transverse but not compressional electromagnetic effects. This reflects the default TGLF setting. For the comparison we chose the radial location  $r/a = 0.5$ . We emphasize that for this test, the uncalibrated TGLF would have produced an ITER profile for which GYRO simulation fluxes would be **zero** (subcritical) at  $r/a = 0.5$ . After all, this was the fundamental motivation for the present research. The choice of radial location for the comparison can be justified by noting that inside this radial value, the fluxes are extremely close to zero. For example, at  $r/a = 0.4$  the deuterium flux is  $Q_D/Q_{GB} \approx 0.14$ . At  $r/a = 0.3$ , this drops to  $Q_D/Q_{GB} < 0.1$ . Conversely, moving to  $r/a \gg 0.5$  reduces the importance of zonal flow stabilization and thus of the recalibration.

For the GYRO simulations, we carried out 6 simulations characterized by three types of fluctuation physics and two level of ion physics. For the fluctuation physics, we performed sim-

ulations with electrostatic (denoted by  $\Phi$ ), electromagnetic with transverse fluctuations (denoted by  $\Phi, A_{\parallel}$ ) and electromagnetic with transverse and compressional fluctuations (denoted by  $\Phi, A_{\parallel}, B_{\parallel}$ ). For the ion physics, we carried out simulations with and without gyrokinetic Helium. All results in terms of average fluxes are summarized in Fig. 29. As explained repeatedly in this work, in the core of ITER the fluxes are weak (compared to modern tokamaks) and thus highly intermittent. Thus, the GYRO datapoints are subject to significant statistical uncertainty. The effective *target* for GYRO is the TGLF result shown as a red dot. Here, it is important to emphasize that the TGLF-SAT1 model includes extra high- $k$  electron transport that is not retained in the low- $k$  GYRO simulations. The point that includes the high- $k$  electron flux is represented by a black dot in the figure. Indeed, there is good clustering of the electromagnetic GYRO simulations about the TGLF-LOW result, which is a significant improvement over the uncalibrated TGLF result. This clearly shows that TGLF-SAT1 is a significantly better predictor of ITER performance than the original TGLF, and that the ITER performance improvement seen in the previous sections is corroborated *post hoc* by these final GYRO simulations.

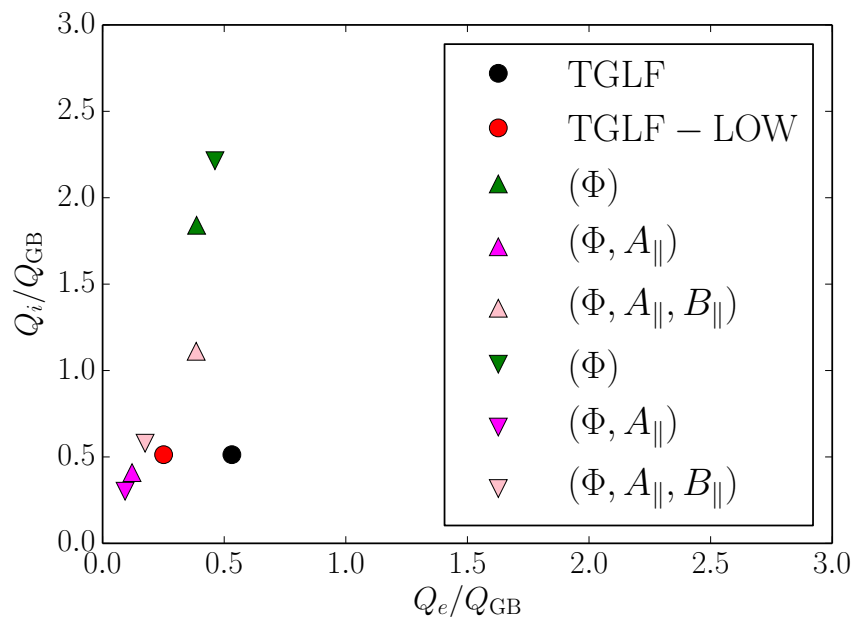


Figure 29: Comparison of full TGLF-SAT1 (black circle) and low- $k$  TGLF-SAT1 (red circle) results compared with GYRO low- $k$  nonlinear simulations. Downward-pointing triangles show GYRO with kinetic (D, T) whereas upward-pointing triangles show GYRO with kinetic (D, T, He). GYRO results are subject to statistical uncertainty due to intermittency. Because TGLF was run with transverse but not compressional fluctuations, the pink triangles are the most appropriate point of comparison with the red TGLF-SAT1 dot.

## **7 Appendix: Summary of GYRO Q2 nonlinear simulations**

$r/a = 0.4$ , weak gradients

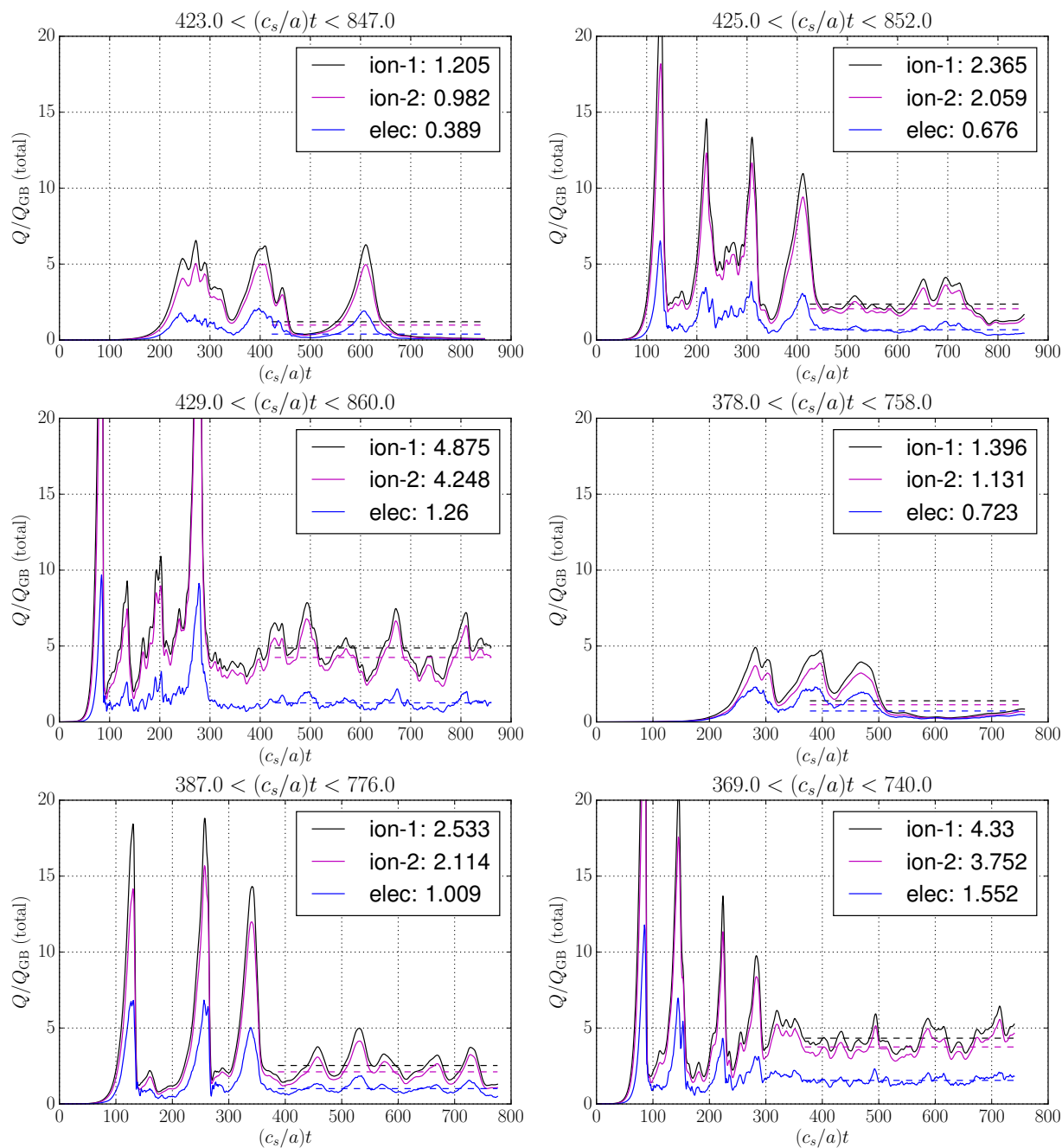


Figure 30: Transport at  $r/a = 0.4$  for weak gradients. Ion 1 is deuterium, ion 2 is tritium.

$r/a = 0.4$ , weak gradients (continued)

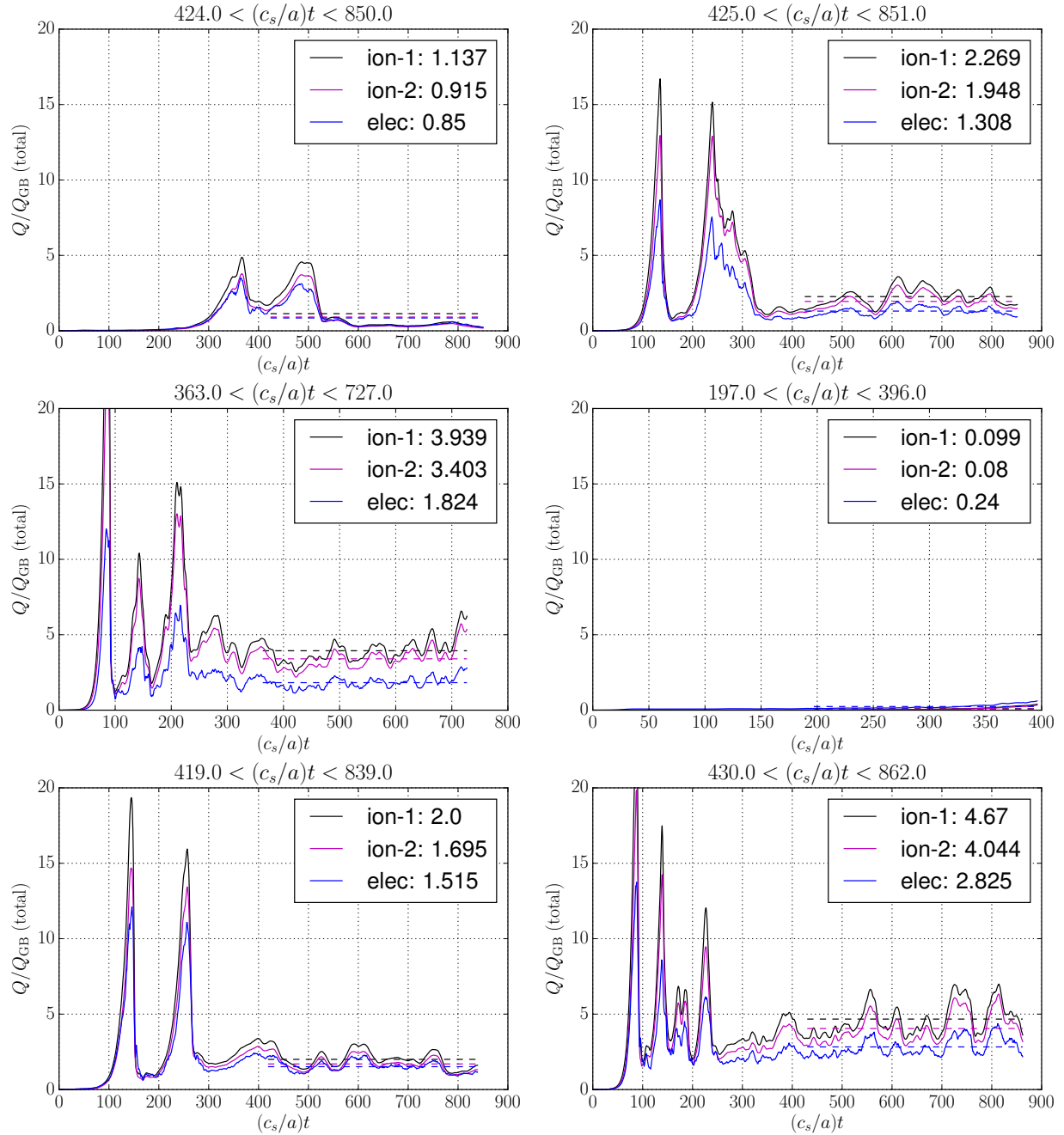


Figure 31: Transport at  $r/a = 0.4$  for weak gradients (continued). Ion 1 is deuterium, ion 2 is tritium.

$r/a = 0.4$ , strong gradients

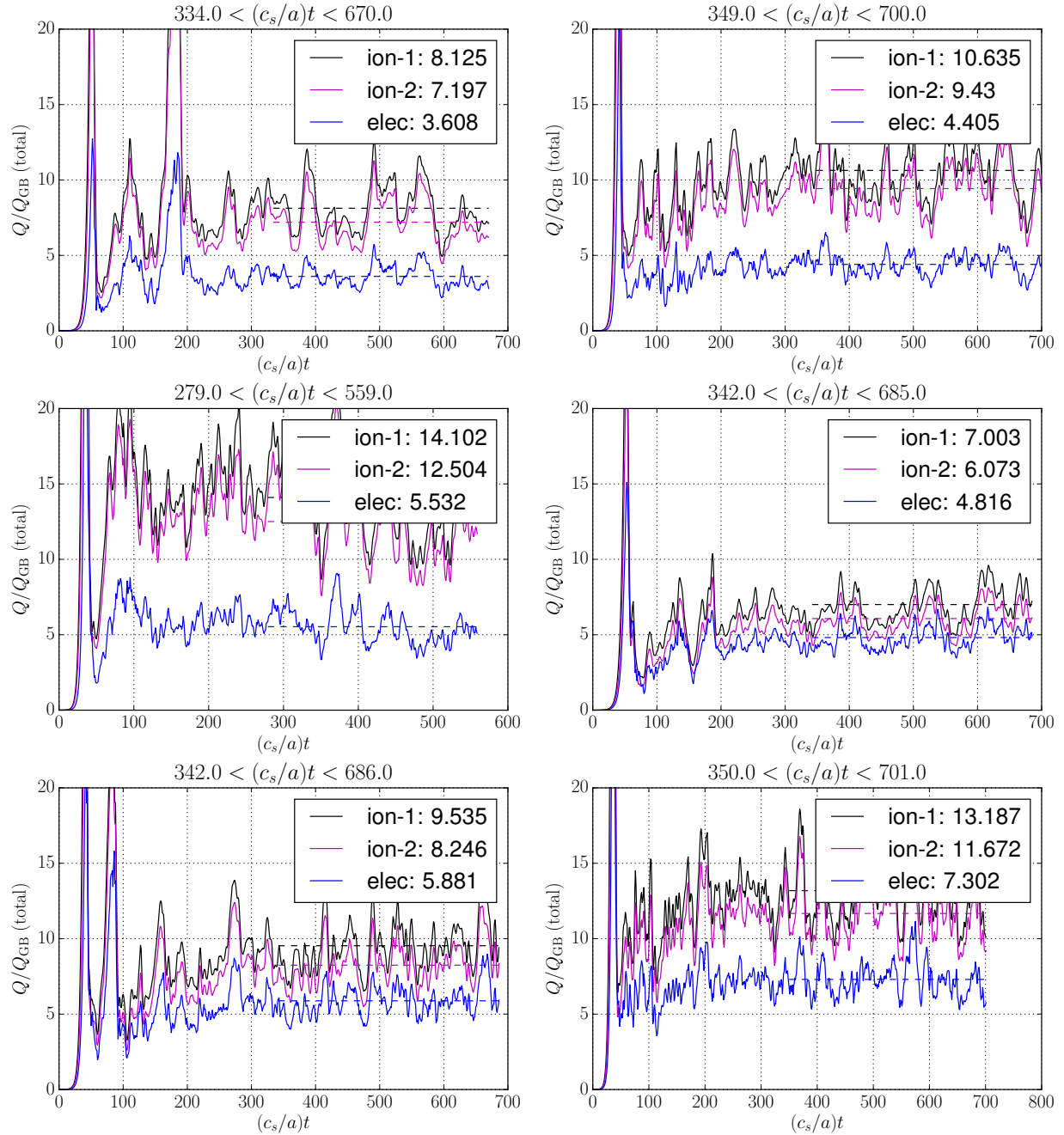


Figure 32: Transport at  $r/a = 0.4$  for strong gradients. Ion 1 is deuterium, ion 2 is tritium.

$r/a = 0.4$ , strong gradients (continued)

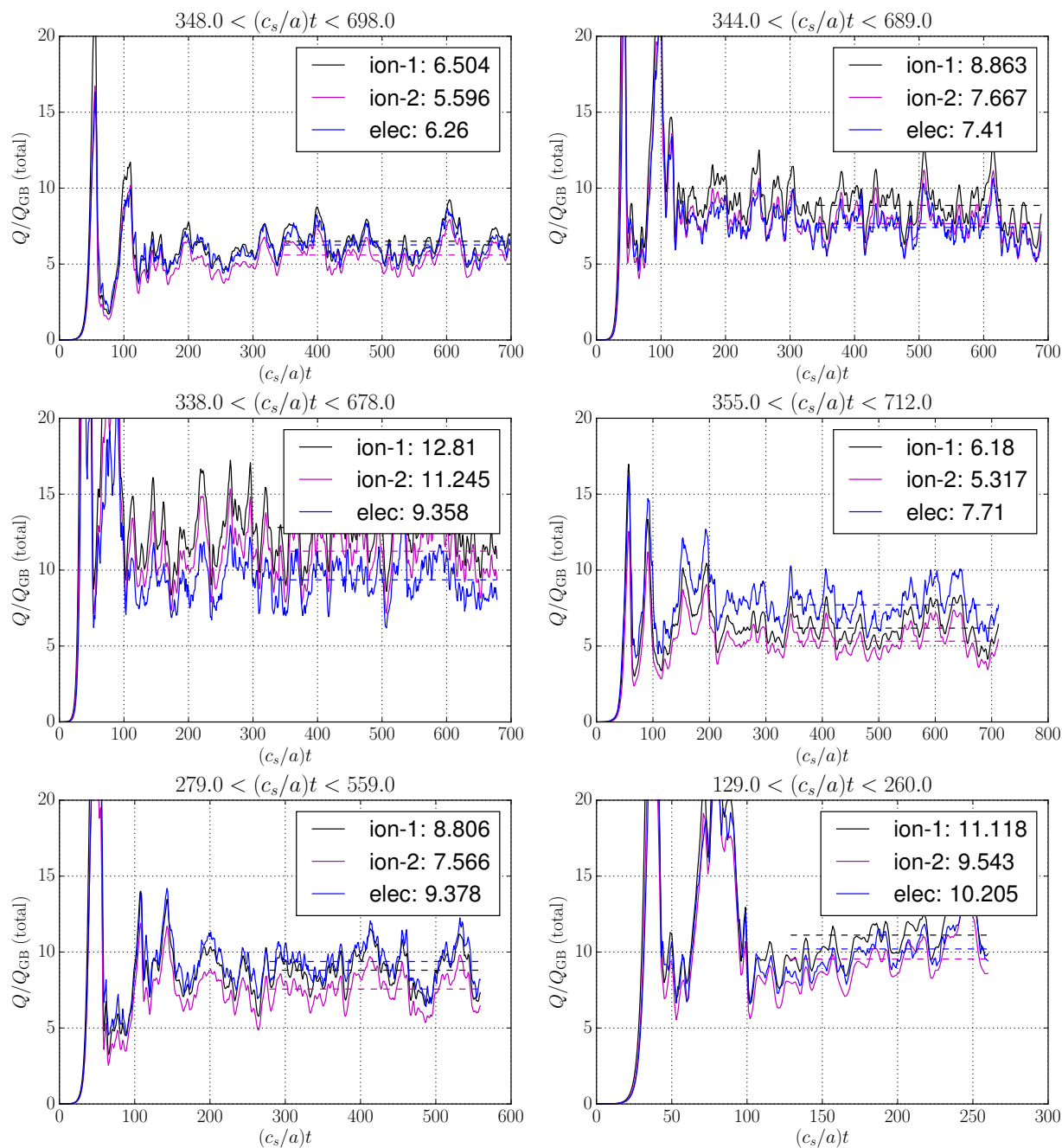


Figure 33: Transport at  $r/a = 0.4$  for strong gradients (continued). Ion 1 is deuterium, ion 2 is tritium.

$r/a = 0.5$ , weak gradients

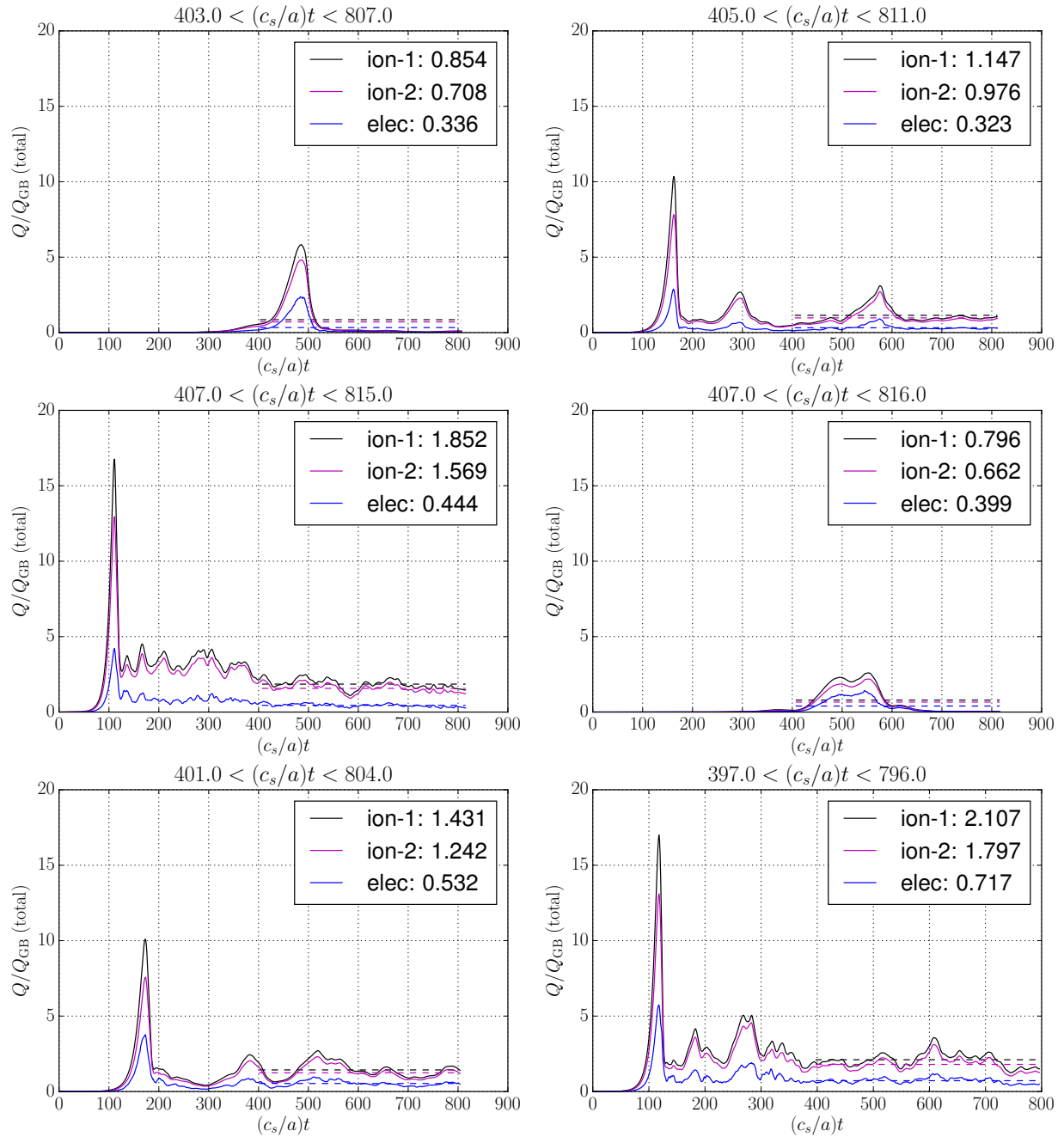


Figure 34: Transport at  $r/a = 0.5$  for weak gradients. Ion 1 is deuterium, ion 2 is tritium.

$r/a = 0.5$ , weak gradients (continued)

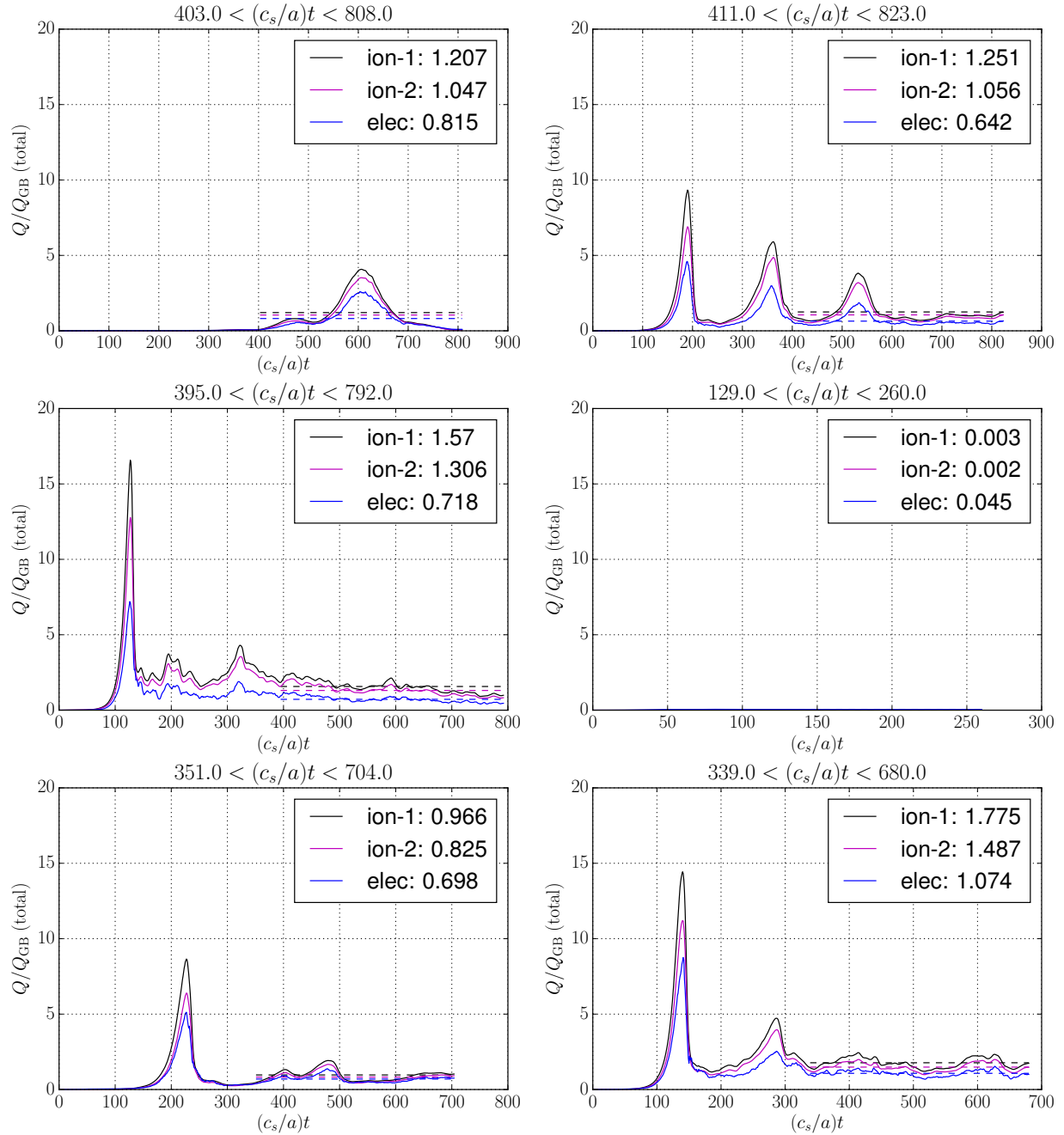


Figure 35: Transport at  $r/a = 0.5$  for weak gradients (continued). Ion 1 is deuterium, ion 2 is tritium.

$r/a = 0.5$ , strong gradients

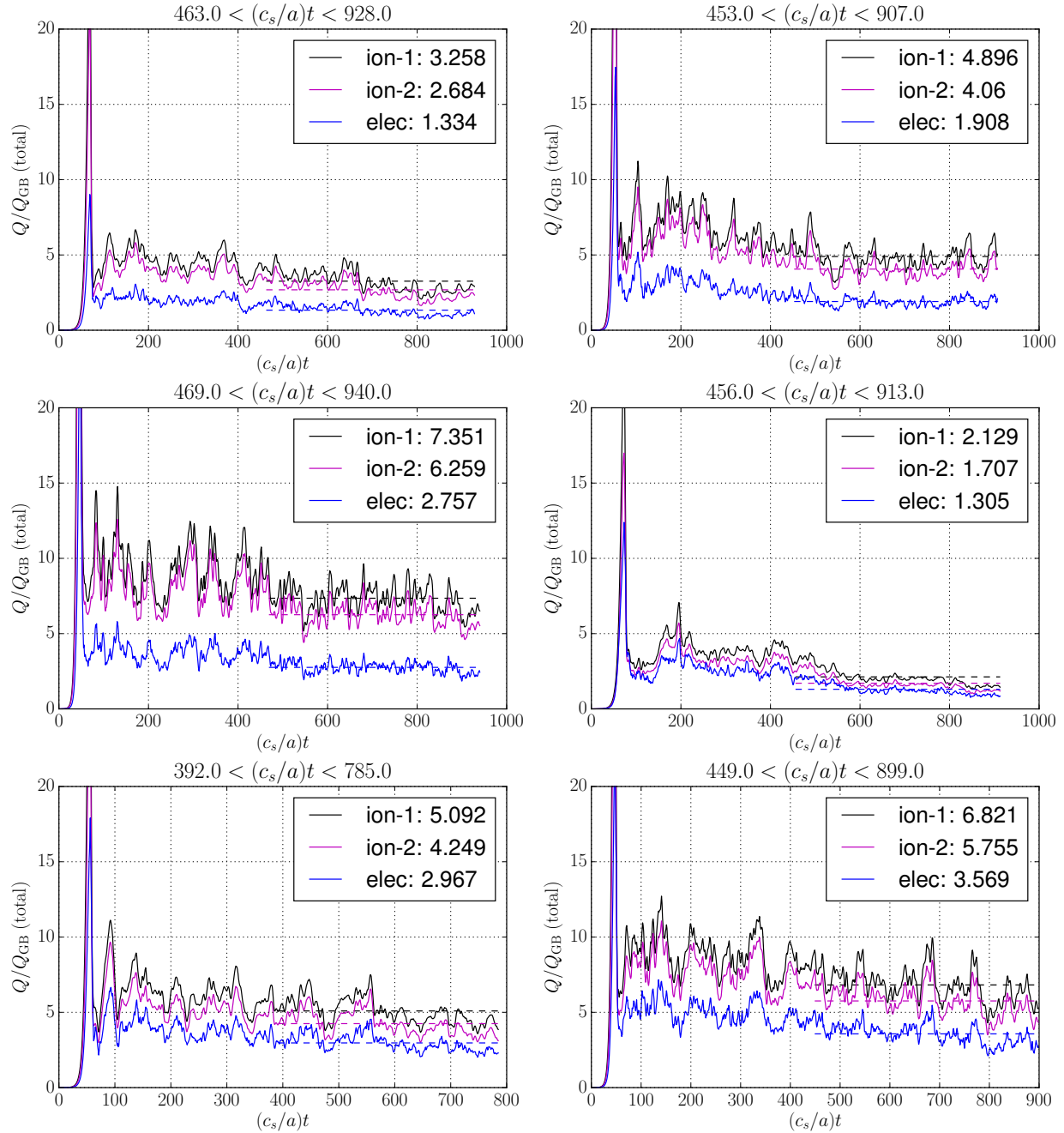


Figure 36: Transport at  $r/a = 0.5$  for strong gradients. Ion 1 is deuterium, ion 2 is tritium.

$r/a = 0.5$ , strong gradients (continued)

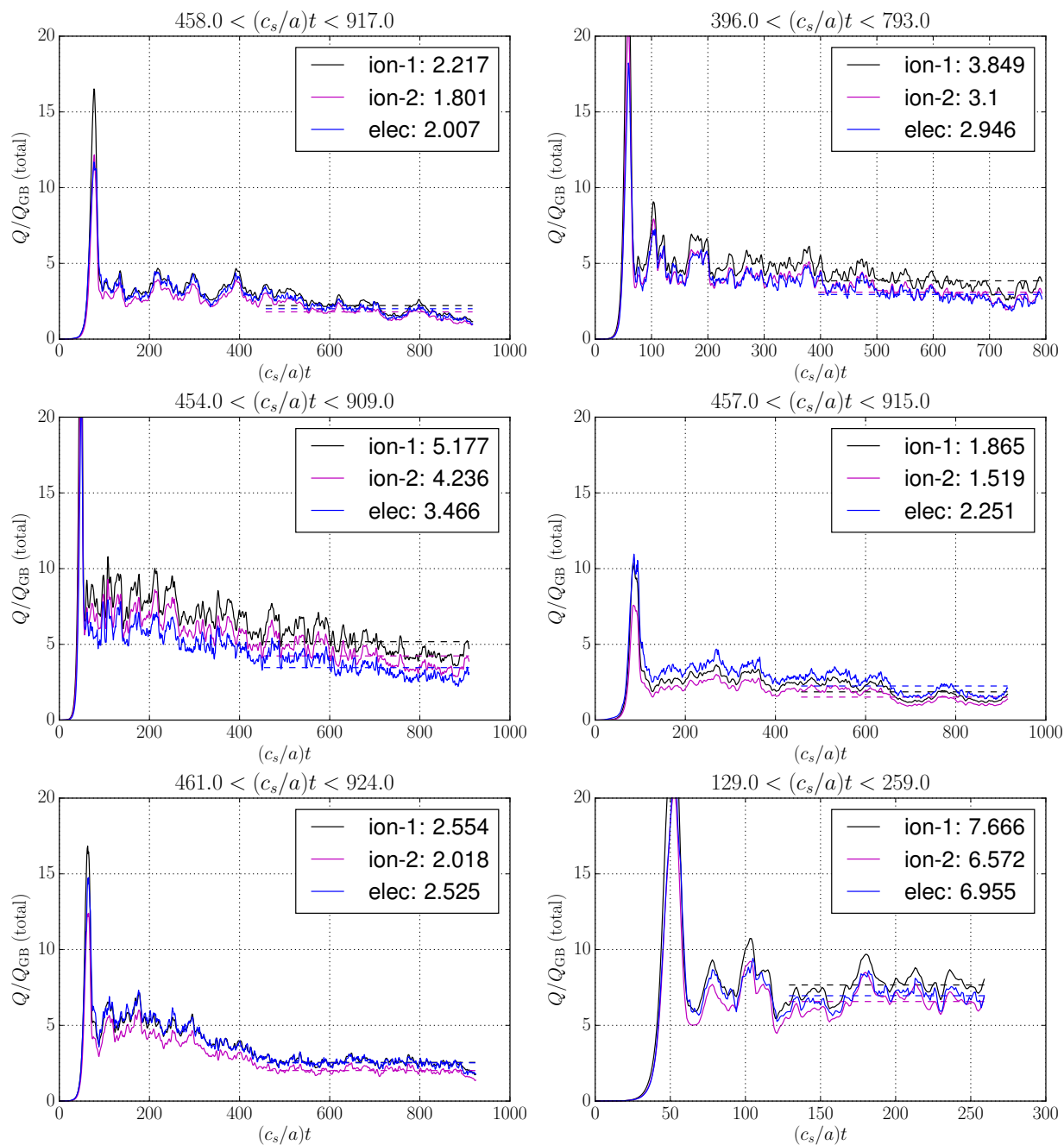


Figure 37: Transport at  $r/a = 0.5$  for strong gradients (continued). Ion 1 is deuterium, ion 2 is tritium.

$r/a = 0.6$ , weak gradients

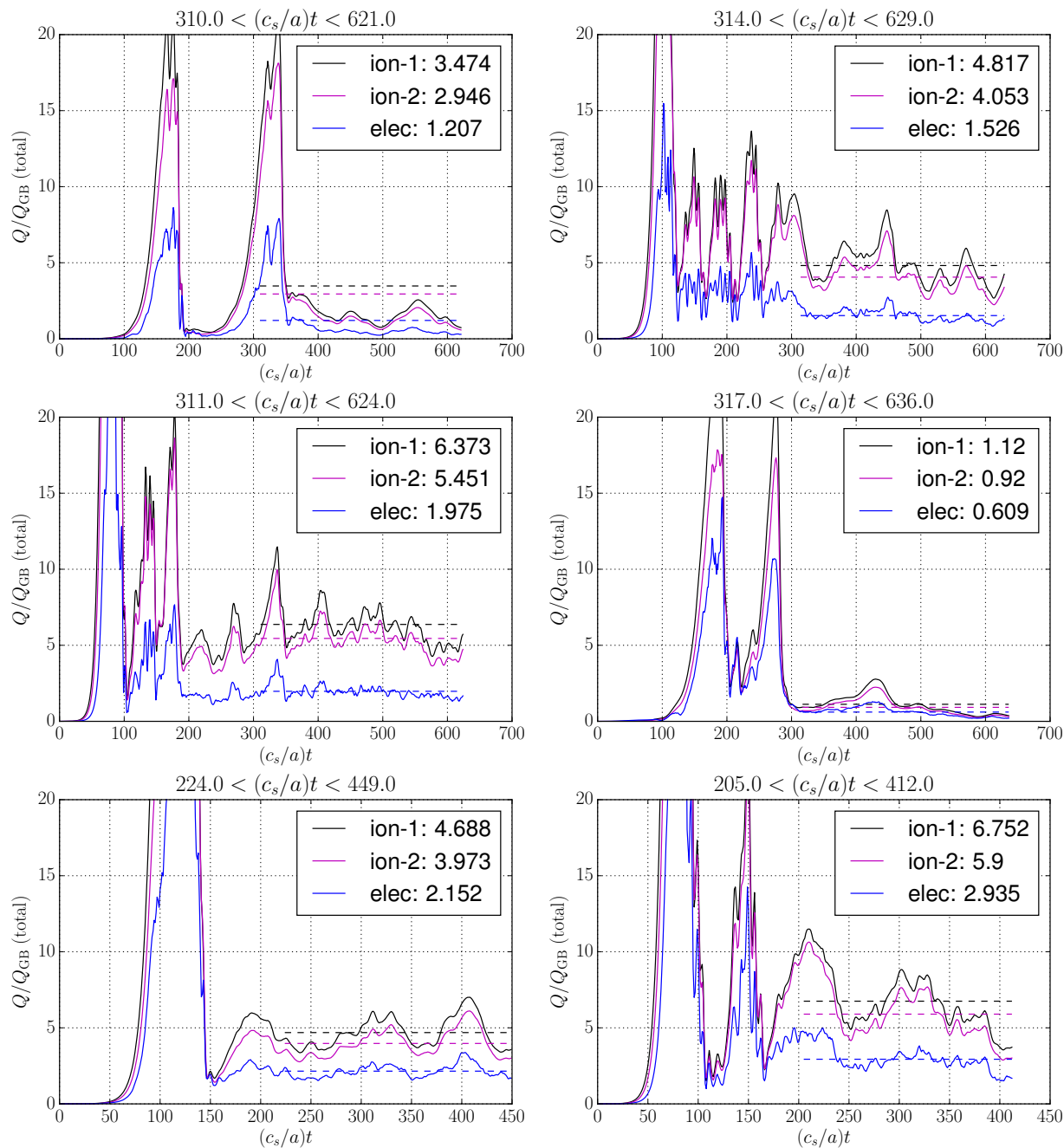


Figure 38: Transport at  $r/a = 0.6$  for weak gradients. Ion 1 is deuterium, ion 2 is tritium.

$r/a = 0.6$ , weak gradients (continued)

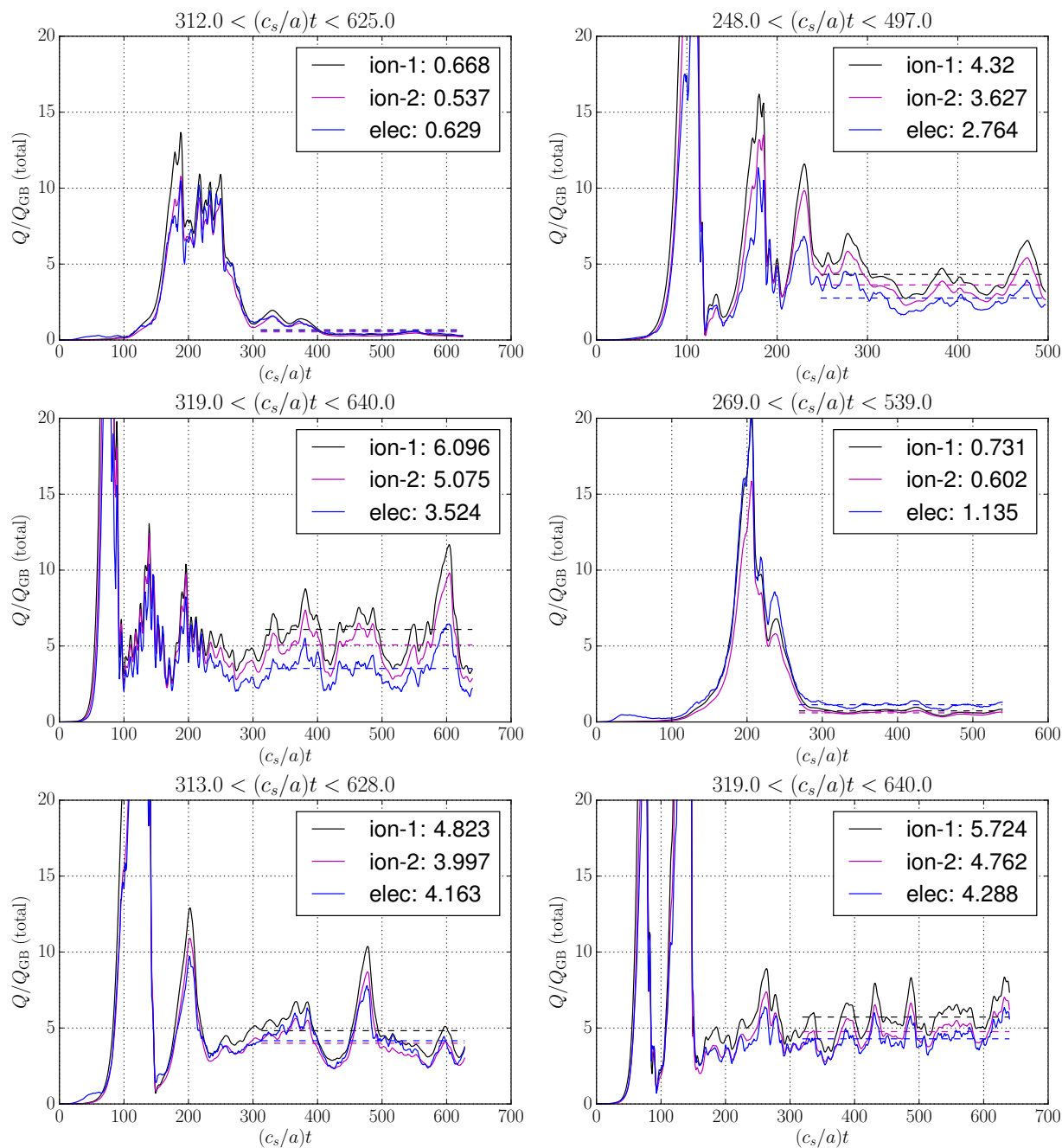


Figure 39: Transport at  $r/a = 0.6$  for weak gradients (continued). Ion 1 is deuterium, ion 2 is tritium.

$r/a = 0.6$ , strong gradients

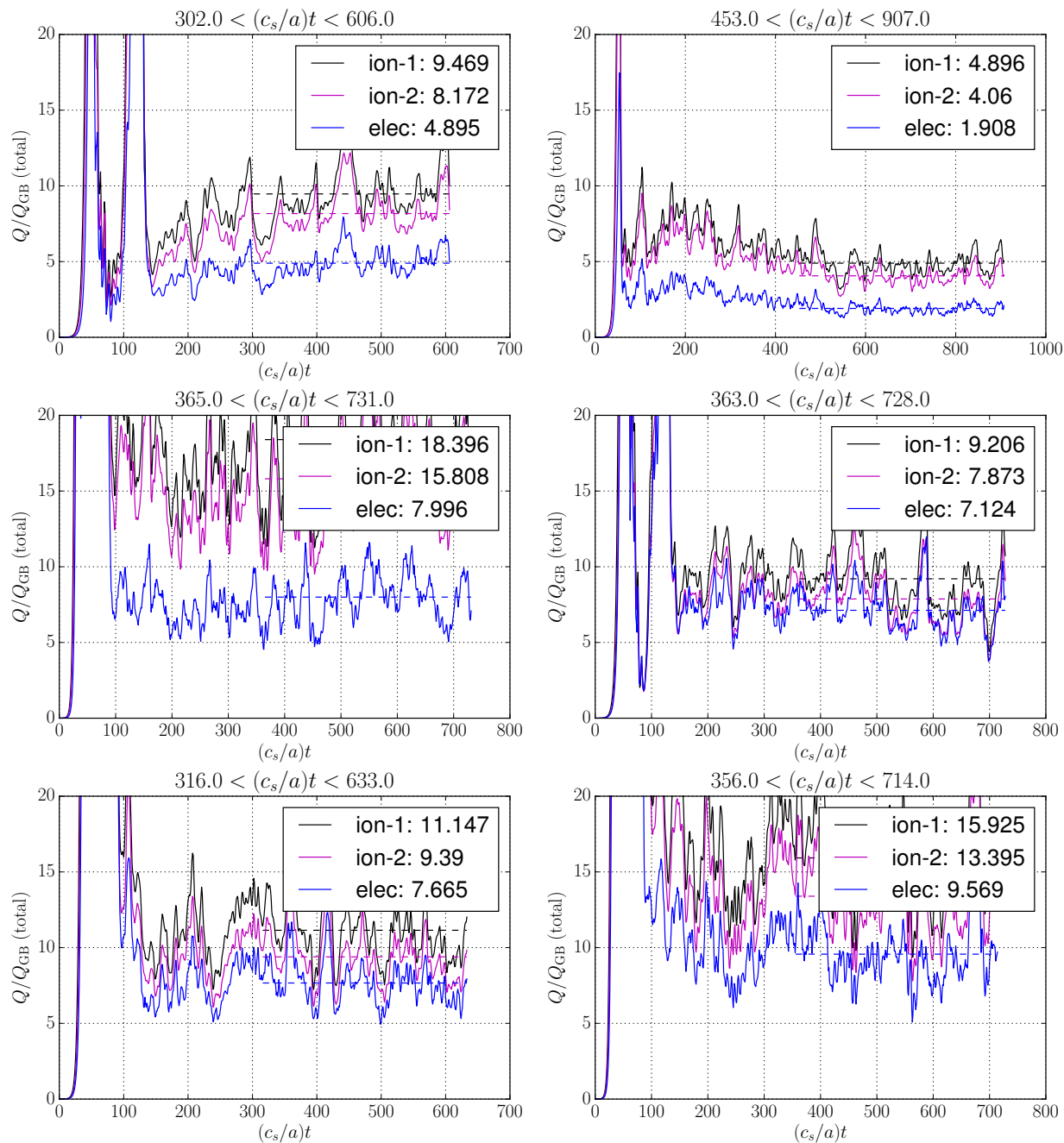


Figure 40: Transport at  $r/a = 0.6$  for strong gradients. Ion 1 is deuterium, ion 2 is tritium.

$r/a = 0.6$ , strong gradients (continued)

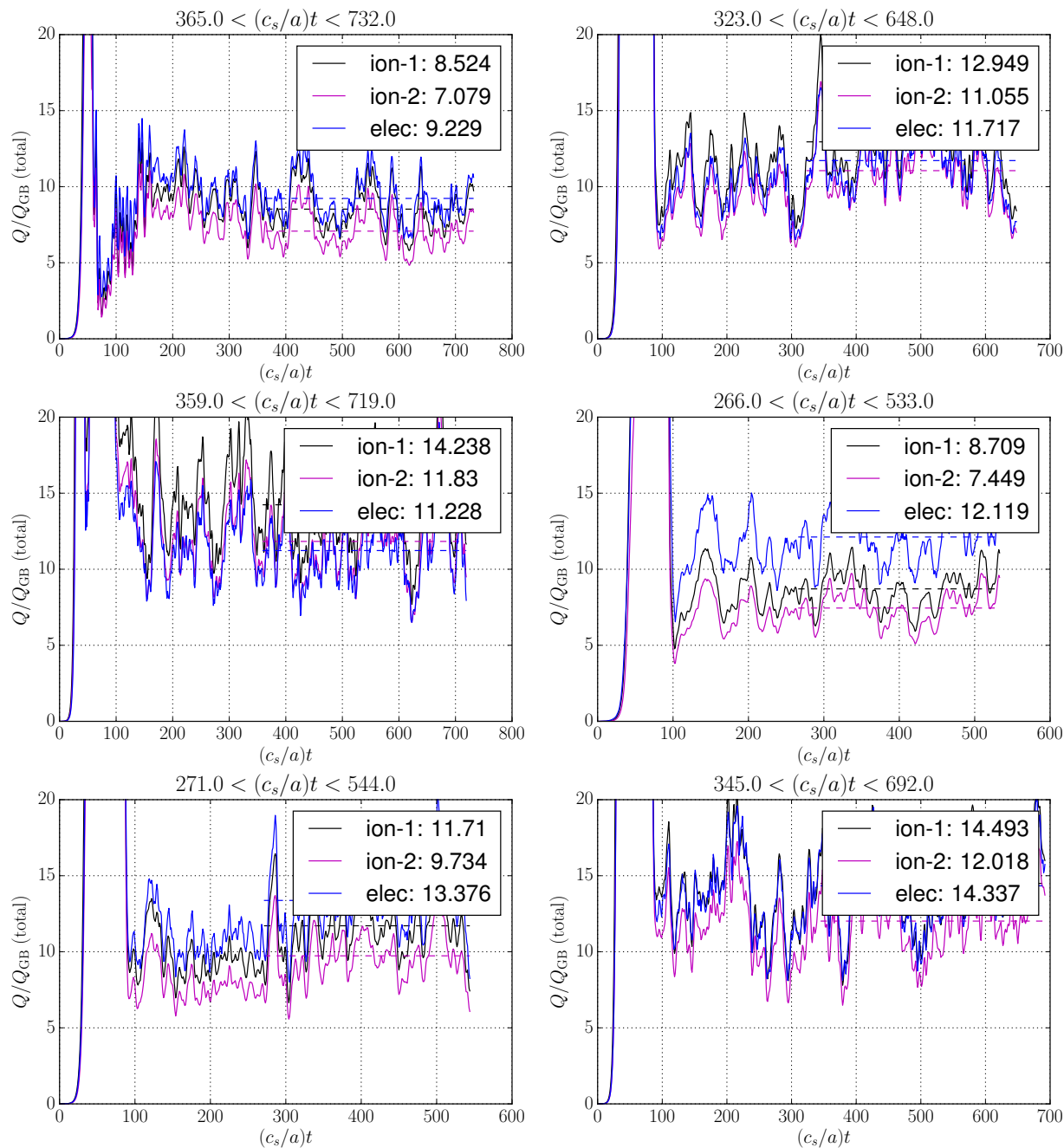


Figure 41: Transport at  $r/a = 0.6$  for strong gradients (continued). Ion 1 is deuterium, ion 2 is tritium.

## References

- [1] J. Candy, R. Waltz, An Eulerian gyrokinetic-Maxwell solver, *J. Comput. Phys.* 186 (2003) 545.
- [2] G. Staebler, J. Kinsey, R. Waltz, Gyro-landau fluid equations for trapped and passing particles, Tech. rep., General Atomics, GA-A24955 (April 2005).
- [3] C. Holland, L. Schmitz, T. Rhodes, W. Peebles, J. Hillesheim, G. Wang, L. Zeng, E. Doyle, S. Smith, R. Prater, K. Burrell, J. Candy, R. Waltz, J. Kinsey, G. Staebler, J. DeBoo, C. Petty, G. McKee, Z. Yan, A. White, Advances in validating gyrokinetic turbulence simulations against L- and H-mode plasmas, *Phys. Plasmas* 18 (2011) 056113.
- [4] I. Pusztai, J. Candy, P. Gohil, Isotope mass and charge effects in tokamak plasmas, *Phys. Plasmas* 18 (2011) 122501.
- [5] C. Holland, C. Petty, L. Schmitz, K. Burrell, G. McKee, T. Rhodes, J. Candy, Progress in GYRO validation studies of DIII-D H-mode plasmas, *Nucl. Fusion* 52 (2012) 114007.
- [6] N. Howard, C. Holland, A. White, M. Greenwald, J. Candy, Synergistic cross-scale coupling of turbulence in a tokamak plasma, accepted for publication in *Physics of Plasmas*.
- [7] G. Staebler, J. Kinsey, R. Waltz, A theory-based transport model with comprehensive physics, *Phys. Plasmas* 14 (2007) 055909.
- [8] J. Kinsey, G. Staebler, R. Waltz, The first transport code simulations using the trapped gyro-landau-fluid model, *Phys. Plasmas* 15 (2008) 055908.
- [9] G. Staebler, J. Kinsey, Electron collisions in the trapped gyro-landau fluid transport model, *Phys. Plasmas* 17 (2010) 122309.
- [10] M. Rosenbluth, F. Hinton, Poloidal flow driven by ion-temperature-gradient turbulence in tokamaks, *Phys. Rev. Lett.* 80 (1998) 724.
- [11] J. Kinsey, G. Staebler, J. Candy, R. Waltz, R. Budny, ITER predictions using the GYRO verified and experimentally validated trapped gyro-landau fluid transport model, *Nucl. Fusion* 51 (2011) 083001.
- [12] A. Dimits, G. Bateman, M. Beer, B. Cohen, W. Dorland, G. Hammett, C. Kim, J. Kinsey, M. Kotschenreuther, A. Kritz, L. Lao, J. Mandrekas, W. Nevins, S. Parker, A. Redd, D. Shumaker, R. Sydora, J. Weiland, Comparisons and physics basis of tokamak transport models and turbulence simulations, *Phys. Plasmas* 7 (2000) 969.

- [13] J. Candy, C. Holland, R. Waltz, M. Fahey, E. Belli, Tokamak profile prediction using direct gyrokinetic and neoclassical simulation, *Phys. Plasmas* 16 (2009) 060704.
- [14] E. Belli, J. Candy, Kinetic calculation of neoclassical transport including self-consistent electron and impurity dynamics, *Plasma Phys. Control. Fusion* 50 (2008) 095010.
- [15] E. Belli, J. Candy, Fully electromagnetic gyrokinetic eigenmode analysis of high-beta shaped plasmas, *Phys. Plasmas* 17 (2010) 112314.
- [16] C. Estrada-Mila, J. Candy, R. Waltz, Gyrokinetic simulations of ion and impurity transport, *Phys. Plasmas* 12 (2005) 022305.
- [17] J. Candy, R. Waltz, M. Fahey, C. Holland, The effect of ion-scale dynamics on electron-temperature-gradient turbulence, *Plasma Phys. Control. Fusion* 49 (2007) 1209.
- [18] G. Staebler, R. Waltz, J. Candy, J. Kinsey, A new paradigm for suppression of gyrokinetic turbulence by velocity shear, *PRL* 110 (2013) 055003.



**GENERAL ATOMICS**

P.O. BOX 85608 SAN DIEGO, CA 92186-5608 (858) 455-3000